

Higher Dimensionality in the Mg–Co–B System: Synthesis and Structure of Incommensurate Composite $Mg_{1+\epsilon}Co_4B_4$

Paul Oftedahl, Gourab Bhaskar, Nawsher J. Parvez, Zhen Zhang, Yang Sun, John Q. Xiao, Thomas Proffen, Oleg I. Lebedev, and Julia V. Zaikina*



Cite This: *J. Am. Chem. Soc.* 2025, 147, 47508–47522



Read Online

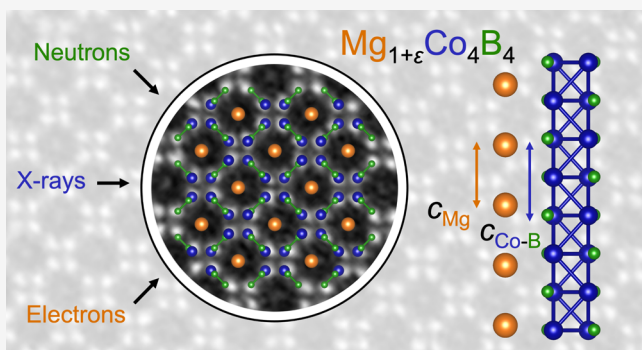
ACCESS |

Metrics & More

Article Recommendations

Supporting Information

ABSTRACT: Guided by high-temperature *in situ* X-ray diffraction, the discovery and synthesis of $Mg_{1+\epsilon}Co_4B_4$ ($\epsilon \approx 0.272$) using a MgH_2 hydride precursor is reported, along with a detailed crystal structure description and measurement of magnetic properties. The mismatch in lattice periodicities between Mg and Co–B substructures places $Mg_{1+\epsilon}Co_4B_4$ in the family of incommensurate composite crystals and prompted structural refinement in a (3 + 1)-dimensional model. The structure of $Mg_{1+\epsilon}Co_4B_4$ ($P4_2/nmc(00\gamma)s00s$, $a = 6.75847(7)$ Å, $c = 3.94007(8)$ Å, $\mathbf{q} = (0, 0, 1.2721(3))$) was refined from neutron powder diffraction and high-resolution powder X-ray diffraction data and confirmed by scanning transmission electron microscopy and electron diffraction. $Mg_{1+\epsilon}Co_4B_4$ is isostructural to $Nd_{1+\epsilon}Fe_4B_4$ and several related ternary borides with $0.07 \leq \epsilon \leq 0.17$, with Mg occupying the rare-earth site. Satellite reflections in the electron diffraction patterns hinted at positional modulation of the transition metal–boron substructure by Mg atoms, but this could not be refined from the neutron or X-ray diffraction data. Low-temperature magnetic measurements show no indications of long-range magnetic ordering or superconductivity down to 5 K. DFT calculations confirmed the absence of a magnetically ordered ground state and the stability of a 5:4 supercell ($\epsilon = 0.25$) relative to the fully commensurate structure. Neutron diffraction and synthesis from elemental Mg demonstrated that $Mg_{1+\epsilon}Co_4B_4$ is not a hydrogen-stabilized phase. $Mg_{1+\epsilon}Co_4B_4$ represents the second compound reported in the Mg–Co–B system and the first superspace symmetry model of a $Nd_{1+\epsilon}Fe_4B_4$ -type incommensurate composite compound refined from powder diffraction data.



INTRODUCTION

The class of intermetallic compounds known as metal borides showcases a wide range of crystal structures, bonding motifs, and functional properties. Among the properties observed in metal boride materials are permanent magnetism,¹ superconductivity,^{2,3} magnetocaloric effect,^{4–6} electrocatalytic activity,^{7–9} and superhardness.^{10–12} Likewise, the diversity of structural chemistry in the boride family is almost unparalleled among crystalline solids,¹³ with the boron substructure adopting motifs anywhere between two extremes of isolated boron atoms and intricate 3-D boron substructures based, among other factors, on the ratio between the metal and boron.^{14,15} On the other hand, rich structural diversity has been seen even for a fixed metal-to-boron ratio. For instance, for metal borides with equal parts metal *M* and B, the boron substructure may range from isolated B_2 and B_3 fragments ($NaIr_3B_4$)¹⁶ and B_4 units and isolated boron atoms ($Ca_2Os_3B_5$)¹⁷ to single zigzag chains (CrB , α -MoB, $NbCoB_2$) and double zigzag chains of boron (Cr_3AlB_4), linear boron chains with isolated boron atoms ($HfIr_3B_4$),¹⁸ and

chains of boron pentagons and isolated boron dimers ($Ta_3Co_4B_7$).¹⁹

The binary boride systems with rare-earth and transition metals have been extensively explored; consequently, most recent synthetic efforts have focused on discovering ternary and higher borides. Recent computational work has predicted ternary borides featuring a first-row transition metal to be promising as electrode materials for Li- and Na-ion-based batteries^{20,21} and to display unconventional magnetic properties such as altermagnetism and quantum spin dimers.^{22–24} Therefore, the search to find new ternary metal borides including a first-row transition element holds promise for a variety of exciting properties and structural motifs.

Received: September 19, 2025

Revised: November 20, 2025

Accepted: November 21, 2025

Published: December 10, 2025



Synthesis of ternary borides containing an alkali or alkaline-earth metal presents considerable challenges to the experimentalist, since conventional synthesis methods like arc-melting and induction heating are impractical due to the high vapor pressure of these metals.²⁵ Only a few ternary borides of the type A-T-B (A = Group 1 or 2 element, T = first-row transition metal) have been synthesized using high-temperature annealing of elemental precursors, and those that were made often required prolonged annealing.^{26,27} The volatility and ductility of A , relatively low reactivity of T , and high melting point of B , as well as the almost complete immiscibility of A and T in most cases present a range of thermodynamic and kinetic factors that hinder the formation of a ternary phase. The kinetic problem of intimately mixing a ductile metal and brittle boron can be overcome by replacing the alkali or alkaline-earth metal A with its hydride AH or AH_2 , a salt-like powder which can be ball-milled with the other powdered precursors before the high-temperature annealing. The extreme reactivity of the hydride allows reactions to occur more quickly at less extreme conditions, improving the chances of forming a metastable phase that may be inaccessible through conventional methods.²⁸ So far, our group has successfully used the hydride route to expand the catalog of known compounds in the Li–Ni–B system^{26,29–31} and to discover the first compound in the Mg–Co–B system.³² In this work we present a second compound in this system: $Mg_{1+\epsilon}Co_4B_4$ ($\epsilon \approx 0.272$), the first example of a synthesized RT_4B_4 -type compound with Mg on the rare-earth site.

Four distinct structure types with the general formula RT_4B_4 are known, where R is one of the 17 rare earth elements (or Th, U, or Pu) and T is a transition metal of groups 7–9. Along with several superstructure and other derivatives, these structures are all characterized by transition metal tetrahedra and isolated boron dimers (Figure 1).³³ The $CeCo_4B_4$ ($P4_2/nmc$) and $LuRu_4B_4$ ($I4_1/acd$) structure types are topologically related and consist of a three-dimensional framework where the R atoms and the centers of the T_4 tetrahedra form a distorted rock-salt array.³³ These two structures differ with respect to the relative orientations and connectivity of the transition metal tetrahedra, as well as the positioning of B–B

dimers within the voids of the framework and the B–B separation within the dimers.³⁴ Another structure type, orthorhombic $LuRh_4B_4$ ($Ccce$), can be seen as a hybrid of the $CeCo_4B_4$ ($P4_2/nmc$) and $LuRu_4B_4$ types.³³ Many such compounds are known to become superconducting or order magnetically at low temperatures, most notably $ErRh_4B_4$ and its substitutional derivatives that display a complex interplay between superconductivity and local-moment ferromagnetism.^{35–37}

The $NdCo_4B_4$ structure type is distinct from the other three in that the T_4 tetrahedra share two opposite edges to form infinite chains along c , which connect along the [110] directions to form octagonal channels containing infinite chains of R atoms (Figure 1d).³³ Although in most cases the T -B and R substructures exhibit the same periodicity along the channel direction, for T = Fe, Mn, and Re the c -parameter of the two substructures may diverge slightly, leading to an incommensurate composite structure.^{38–40} For the archetypal case of $Nd_{1+\epsilon}Fe_4B_4$, there is evidence that the ratio between the c -parameters of the two substructures may take on arbitrary values within a certain range.⁴¹ Zhao and Hong enumerated the symmetry requirements both for arbitrarily large supercells and an incommensurate composite model of $Nd_{1+\epsilon}Fe_4B_4$ -type structures in superspace.⁴² The structures of many $Nd_{1+\epsilon}Fe_4B_4$ -type phases have been solved using commensurate supercell approximants, while the recent work of Stöger et al. on $Y_xOs_4B_4$ represents the only refinement of a $Nd_{1+\epsilon}Fe_4B_4$ -type phase using the more streamlined superspace approach.⁴³

Aperiodic crystals are solids which do not adhere to the traditional requirement that a crystal display translational symmetry along three spatial axes, but whose structure is completely ordered when a higher-dimensional symmetry is introduced.⁴⁴ Aperiodic crystals are divided into three types: incommensurately modulated crystals, incommensurate composite crystals, and quasicrystals. In an incommensurately modulated crystal, atomic structure factors may be modified according to a “modulation vector” at least one of whose components is not related to the unit cell length by a rational fraction. An incommensurate composite crystal consists of two (or more) substructures that share a common periodicity along one or more crystallographic axes but whose periodicities differ along at least one axis. The ratio between the conflicting periodicities cannot be approximated by a rational fraction, so one or more modulation vectors are introduced to establish the relative periodicities. In addition, such structures often (but not necessarily) display modulation in accord with this incommensurate vector whereby the structure factors of one composite part are modulated according to the periodicity of the other.⁴⁴

Such solids are indeed crystalline, i.e., they exhibit long-range order, as evidenced by the fact that their diffraction patterns consist of sharp Bragg peaks,⁴⁵ yet they are not periodic, in that one unit cell and a basis set of direct space translation vectors does not suffice to describe the entire crystal. Consequently, the set of Bragg peaks that constitutes the diffraction pattern of such solids cannot be indexed simply by a basis set of three vectors in reciprocal space, so additional vectors q_i are introduced to give a set of $(3 + d)$ integers that are adequate to index all observed reflections (d representing the requisite number of vectors q_i). Formally, these additional vectors are projections of vectors in higher-dimensional space onto 3D reciprocal space, while the crystal itself is understood as an intersection of 3D direct space with a higher-dimensional

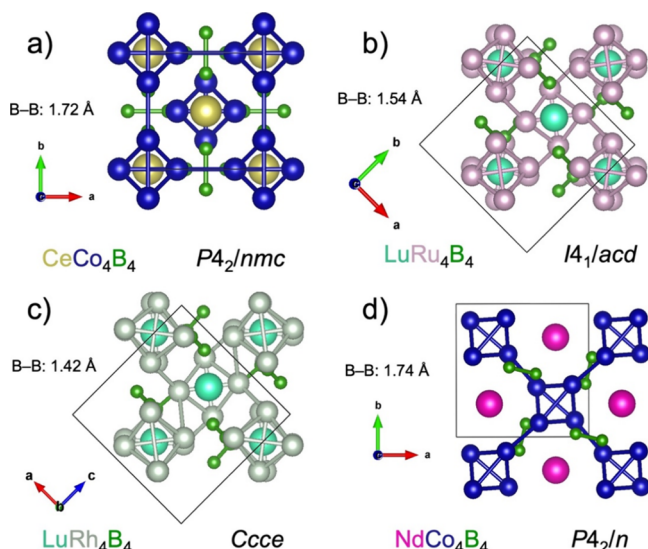


Figure 1. Comparison of RT_4B_4 structure types: (a) $CeCo_4B_4$, (b) $LuRu_4B_4$, (c) $LuRh_4B_4$, and (d) $NdCo_4B_4$.

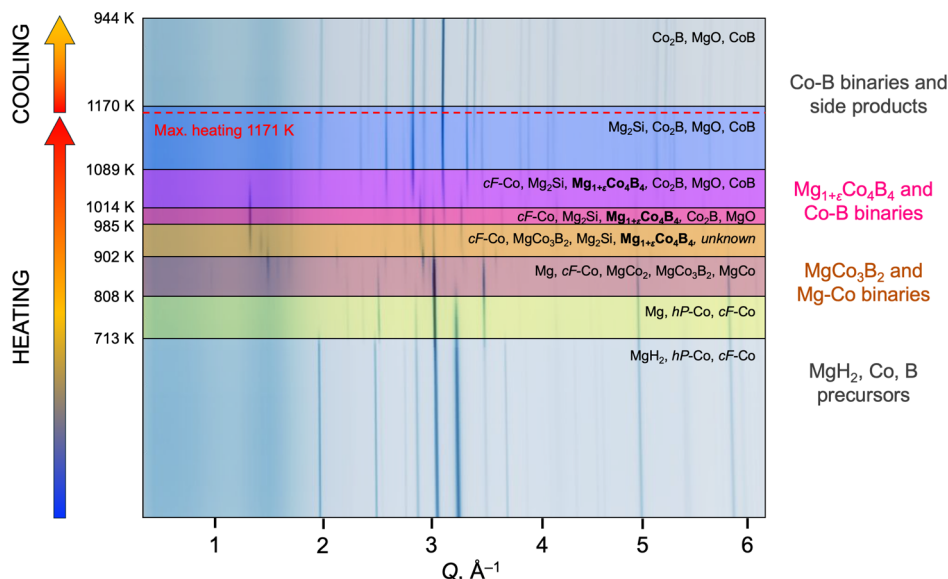


Figure 2. Temperature-resolved in situ PXRD of a precursor mixture containing powders of MgH₂, Co, and B in a 1.5:1:4 ratio. Each horizontal section represents a PXRD pattern where darker shading represents higher diffraction intensity. Temperature regions where previously unknown phases are observed are colored orange, fuchsia, and purple; selected patterns from these regions are compared with calculated patterns in Figure S1. Data were collected at beamline 11-ID-C APS ANL at wavelength $\lambda = 0.11595 \text{ \AA}$.

space where translational periodicity of the crystal is recovered. These higher dimensions are merely a mathematical formalism, as implied by the notation of such structures as $(3 + d)$ -dimensional, where the higher dimensions $d = 1, 2$, or 3 are conceptually distinct from the 3 ordinary spatial dimensions.

In this work, we report the synthesis, crystal structure, and magnetic properties of Mg_{1+ε}Co₄B₄, a novel compound adopting an incommensurate composite structure isostructural to Nd_{1+ε}Fe₄B₄. The structural model was refined in $(3 + 1)$ -dimensional superspace using powder X-ray and neutron diffraction data and confirmed with electron diffraction and scanning transmission electron microscopy.

EXPERIMENTAL SECTION

Synthesis of Mg_{1+ε}Co₄B₄ utilized a high-temperature reaction of powders of MgH₂, Co, and B, with isotopically pure ¹¹B used for the neutron diffraction sample. Excess Mg turnings and presynthesized CoB powder were used as precursors for single-crystal growth. For polycrystalline Mg_{1+ε}Co₄B₄, precursors were sealed in a Nb crucible under argon atmosphere, placed in an evacuated silica reactor and heated in a box furnace to 1173 at 1.8 K/min, held at that temperature for 36 h, and cooled by turning off the furnace. Most samples were washed with dilute aqueous HCl ($\text{pH} > 2$) following annealing to remove unreacted Mg. Powder X-ray diffraction (PXRD) measurements were collected on a Rigaku MiniFlex600 powder diffractometer with Cu K_{α} radiation ($\lambda = 1.54051 \text{ \AA}$), and single-crystal X-ray diffraction measurements were obtained using a Bruker D8 Venture diffractometer equipped with a Mo- μ S microsource. Variable-temperature synchrotron PXRD was acquired at beamline 11-ID-C ($\lambda = 0.11595 \text{ \AA}$) for unreacted MgH₂, Co, and B precursors, and at beamline 17-BM ($\lambda = 0.24110 \text{ \AA}$) for the prereacted Mg_{1+ε}Co₄B₄ powder, both at the Advanced Photon Source (APS) at Argonne National Laboratory (ANL). Room-temperature time-of-flight neutron powder diffraction data were collected at beamline BL-11A (POWGEN)⁴⁶ of the Spallation Neutron Source (SNS) at Oak Ridge National Laboratory (ORNL). Room-temperature high-resolution synchrotron PXRD was collected at the Low-Energy Wiggler (LEW) beamline ($\lambda = 0.81931 \text{ \AA}$) of the Brockhouse Diffraction Sector (BDS) at the Canadian Light Source (CLS). High-angle annular dark-field scanning transmission electron microscopy

(HAADF-STEM) images and Electron Diffraction (ED) patterns were obtained on a JEM ARM200F cold FEG double aberration-corrected microscope operated at 200 kV; for measurement, polycrystalline Mg_{1+ε}Co₄B₄ sample was ground with ethanol in an agate mortar to form an ethanolic suspension that was deposited on a Cu holey carbon grid. Density functional theory (DFT) calculations were conducted using VASP employing the projector augmented wave (PAW) method.^{47–50} The LOBSTER program was used to calculate projected and integrated crystal orbital Hamilton populations (COHP).^{51–54} Magnetic property measurements were obtained using a Quantum Design PPMS DynaCool 12T magnetometer on polycrystalline samples sealed between two rods in an EPR tube under vacuum. Additional details of the experimental methods used can be found in the Supporting Information.^{55–63}

RESULTS AND DISCUSSION

Synthesis. Recently, our group reported on the use of in situ high-temperature powder X-ray diffraction (PXRD) to discover MgCo₃B₂, the first compound to be reported in the Mg–Co–B system.³² Predictions of quantum phenomena in AMB₄ compounds prompted us to explore the B-rich region of the Mg–Co–B system using in situ PXRD.^{22,23} In an experiment with initial composition 1.5MgH₂ + Co + 4B, we observed two distinct sets of unknown peaks as well as peaks corresponding to known binary and ternary phases. The observed sequence of phase transformations between 808 K and 1089 K closely resembles an in situ experiment reported for the Mg–Fe–B system with composition 1.3MgH₂ + Fe + 4B.²² The first set of unknown peaks (labeled as “unknown” in Figure S1) is not observed in the previously reported Mg–Co–B in situ reaction with a higher Co:B ratio;³² this phase forms at higher temperatures (902–985 K) than MgCo₃B₂. This phase has not been seen in ex situ experiments; we hypothesize that it may be a hydride or hydrogen-stabilized phase that requires significant partial pressure of H₂ to form. The second set of unknown peaks is also observed at higher temperatures (902–1089 K) than MgCo₃B₂, which guided our ex situ reactions into the higher-temperature and boron-rich region of compositional space. Rapid screening using the

hydride route enabled us to synthesize a phase with peaks that matched those of the *in situ* experiment at 985 K (**Figure S1**). To determine the structure of this phase (later found to be $Mg_{1+\epsilon}Co_4B_4$), we performed a single-crystal growth using excess elemental Mg to serve as a flux and a slow cooling step, followed by centrifugation to separate the excess molten Mg from the ternary phase.

Two structural solutions were obtained from single-crystal X-ray diffraction (SCXRD), both related to the $NdCo_4B_4$ structure type with chains of Co_4 tetrahedra forming a framework that hosts Mg atoms inside infinite channels along the *c*-direction. Further details of the SCXRD refinements and models can be found in the **Supporting Information (Note S1, Tables S1–S3)**. The model with more realistic interatomic separations and a better match to laboratory PXRD data is a commensurate supercell of the $Nd_{1+\epsilon}Fe_4B_4$ type with composition $Mg_5Co_{16}B_{16}$. This compositional information permitted further synthesis optimization of polycrystalline powder samples using the hydride route. Although the phase was observed to form across a wide range of compositions and temperatures, the optimized synthesis is performed at 1173 K with a dwell time of only 36 h. A loading composition of equimolar amounts of MgH_2 , Co, and B was used for all the samples measured in this work, except for two of the samples prepared for magnetometry, as described in the Experimental section. An excess of the alkali or alkaline-earth hydride precursor is often required to avoid admixtures of transition metal–boron binary compounds. In this case, however, a considerable amount of elemental magnesium remained after the annealing which was removed by treatment with mild aqueous HCl for samples used for diffraction experiments (see the **Experimental Section**).

Several considerations should be kept in mind relative to the synthesis of samples of $Mg_{1+\epsilon}Co_4B_4$ on which the diffraction measurements discussed in the remainder of the paper were performed. As noted above, an excess of elemental Mg was used for single crystal growth, since we have found that hydride precursors tend to lead to microcrystalline samples with crystals too small for laboratory SCXRD. The successful synthesis of the target phase from elemental Mg, together with the neutron diffraction results (*vide infra*), demonstrate that hydrogen does not play a role in the stabilization of the target compound. Neutron diffraction is often used to locate light elements such as hydrogen, boron, and carbon, which are weak X-ray scatterers.^{64,65} However, ^{10}B is a strong neutron absorber, so isotopically enriched ^{11}B must be obtained to prepare samples for neutron scattering experiments. Samples prepared by these three different precursor combinations yielded structural models that are all in close agreement. In particular, the nearly identical values of modulation vector \mathbf{q} for the high-resolution PXRD and neutron diffraction models demonstrate that the composition of the phase does not vary depending on the specific boron source used for synthesis (*vide infra*).

Refinement of Commensurate Models Against Powder Diffraction. While the SCXRD solution with composition $Mg_5Co_{16}B_{16}$ yielded a plausible structural model, the refinement gave high residual values and physically unreasonable atomic displacement parameters. Furthermore, the low overall intensity of reflections and a large number of unindexed reflections pointed to poor crystal quality with extensive twinning. Due to the inadequacy of the available crystals, high-resolution powder diffraction data was used to

further refine the existing structural model. In addition to high-resolution synchrotron X-ray powder diffraction (HR-PXRD) data, neutron powder diffraction (NPD) data were obtained to aid in the determination of positions of light B atoms, which scatter X-rays very weakly.

Rietveld refinement of the $Mg_5Co_{16}B_{16}$ orthorhombic structure model against HR-PXRD revealed a discrepancy related to reflections indexed $hk5$ (**Figure S2** and inset). It became apparent that all such peaks of type $hk5$ were shifted to slightly higher angles with respect to the positions predicted by the model, although the peak intensities were generally in good agreement (**Figure S3**). The same issue was observed in the NPD refinement of the orthorhombic supercell. In effect, the *c*-parameter appeared to be slightly shorter for $hk5$ peaks. Since one unit cell of this model contains four chains of five Mg atoms each, equally spaced along the *c*-direction, the scattering intensity of these $hk5$ peaks is mostly due to the Mg sublattice. Therefore, we hypothesize that a slight decrease in the spacing of the Mg atoms along the *c*-direction would allow the positions of these peaks to be modeled correctly.

Determination of an Incommensurate Composite Model. To construct such a model, we used the indexing and measured *d*-spacings of these peaks to calculate an effective *c*-axis of 15.5148 Å for the Mg substructure, leading to a Mg–Mg separation of 3.10 Å. The ratio of this Mg–Mg separation to the repeating unit of the Co–B substructure (15.747 Å/4 = 3.937 Å) is 0.7875…, for which the smallest rational approximation within 1% is 11/14 = 0.7857. Such a supercell would contain 204 atoms and would be challenging to refine from powder diffraction data. A more efficient approach is to construct a composite model where independent cells for the Mg and Co–B substructures, containing 2 and 16 atoms, respectively, are related by a modulation vector that may be rational or irrational. An incommensurate relation between rare earth and transition metal–boron substructures has been reported for several compounds of the type $R_{1+\epsilon}Fe_4B_4$, but in most cases, the relation between the two substructures can be given by a simple rational fraction, e.g., 8/7 in the case of $Gd_8Fe_{28}B_{28}$, and the compounds were modeled as a superstructure.^{38–40,66}

According to this hypothesis, our compound would fall into the category of “incommensurate composite crystal,” a type of aperiodic crystalline matter where two substructures share a common periodicity along one or more crystallographic axes but whose periodicities differ along at least one axis where the ratio between these periodicities cannot be approximated conveniently by a rational fraction. The formalism for dealing with such structures involves adding an additional crystallographic dimension for each 3D axis for which the periodicities of the two substructures do not align. In our case, the shared *a* and *b* parameters of the two substructures lead to a (3 + 1)-dimensional structure where the added dimension in superspace represents the periodicity of Mg in the [001] direction. The simplest unit cells for the first and second substructures contain, respectively, two Co_4 tetrahedra with eight nearby B atoms, and two Mg atoms. Repetition of these units along *c* gives rise to four columns, while B atoms from neighboring cells connect to form B–B dimers. The cell containing Co and B atoms was chosen to constitute the first substructure, while Mg atoms were assigned to the second substructure. The Co–B subcell is identical to the set of Co and B atoms contained in one unit cell of the small tetragonal $P4_2/nmc$ SCXRD model; initial coordinates of Co and B were borrowed from this model

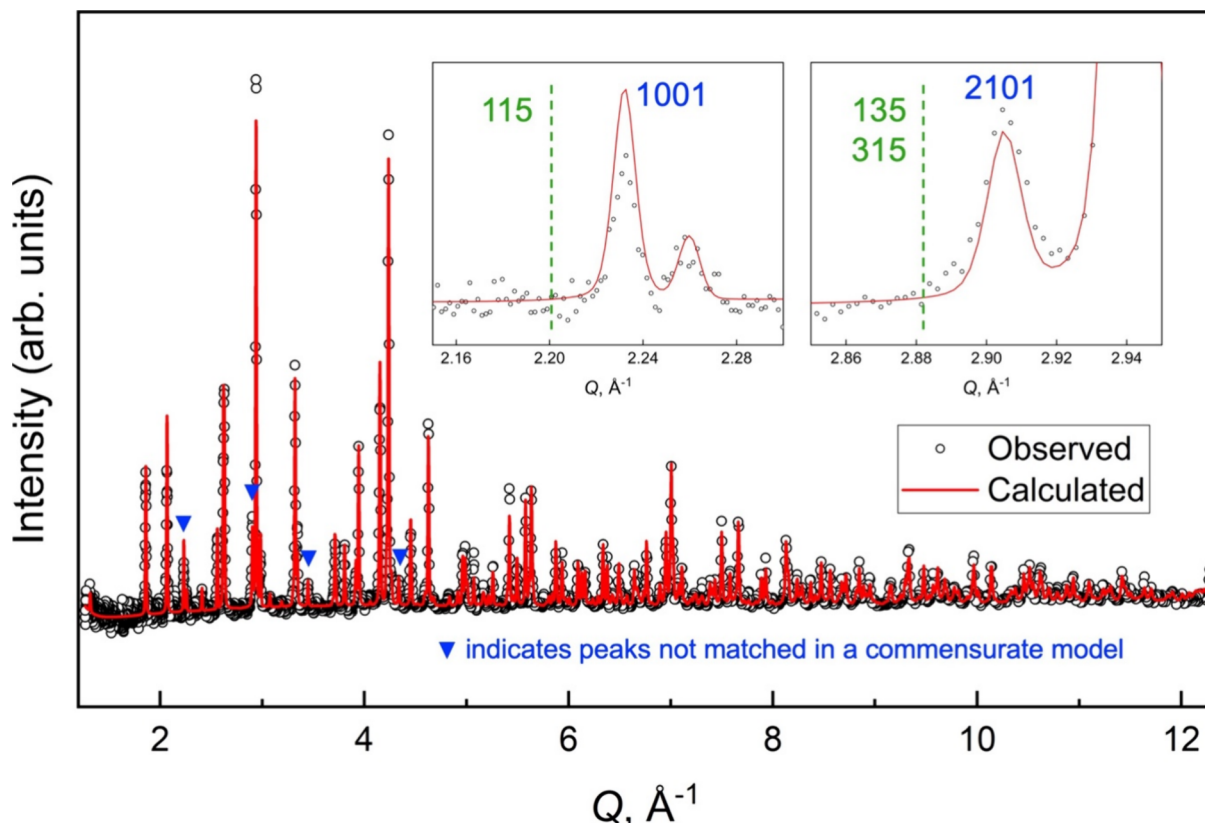


Figure 3. Comparison of observed neutron powder diffraction data (POWGEN, SNS, ORNL) with the calculated profile of the incommensurate composite structural model from Rietveld refinement. The abscissa have been converted from time-of-flight to Q using parameters listed in Table S4. Blue triangles mark the positions of peaks that are approximately indexed $hk\bar{5}$ in the commensurate model that correspond to the Mg substructure. These peaks must be indexed as $h'k'01$ in the superspace model to match their positions correctly. Insets to the main figure with close-ups of two such peaks show that their position is well modeled by the incommensurate composite model (compare to the mismatch in Figures S2 and S3) with dotted lines to show peak positions and indexing according to the commensurate supercell (green) and indexing according to the incommensurate composite structure (blue).

(Table S2). Both atom types occupy special $8i$ Wyckoff sites (x, x, z) in $P4_2/nmc$ (assuming setting #2, origin at inversion center); the multiplicity of these atoms is not affected by embedding the structure in superspace. From the orthorhombic supercell model, it was presumed that Mg atoms form a body-centered tetragonal array as in the NdCo_4B_4 structure ($P4_2/n$); such an array is not possible in the higher 3D symmetry of $P4_2/nmc$ but can be restored by the choice of intrinsic translations $s00s$ when embedding the structure in superspace.

The connection between these two substructures is provided by the modulation vector. In general, a modulation vector will take the form $\mathbf{q} = \alpha\mathbf{a}^* + \beta\mathbf{b}^* + \gamma\mathbf{c}^*$ with respect to the three reciprocal basis vectors in 3D. In the case at hand, since the a and b parameters are shared between both substructures, the modulation vector may not have components along these axes, i.e., $\alpha = \beta = 0$. The magnitude of the modulation vector $|\mathbf{q}|$ is essentially a ratio between the reciprocal lattice parameters c_i^* of the two substructures $i = 1, 2$, while the superspace symmetry group was obtained from the 3D space group by determining the intrinsic translations in the x_4 coordinate necessary to obtain the appropriate Mg substructure and confirmed by the observed systematic absences. The $(3+1)D$ space group of $\text{Mg}_{1+\epsilon}\text{Co}_4\text{B}_4$ is $P4_2/nmc(00\gamma)s00s$, where (00γ) denotes the form of the modulation vector and intrinsic translations $s00s$ correspond to translation of the Mg substructure by $1/2 c_2$ after applying x_1 and x_2 components

of the 4_2 screw axis and m mirror plane. The induced superspace group of the Mg substructure is $P4_2/nmc(00\gamma)s0s0$ (origin choice 2), in which the Mg site $(\frac{3}{4}, \frac{1}{4}, \frac{1}{4})$ has the appropriate 2-fold multiplicity (Wyckoff site $2b$). Further details about determining the modulation vector and superspace symmetry can be found in the Supporting Information (Note S2 and Figure S4).^{67–70}

For $(3+1)D$ crystals consisting of two substructures and one modulation vector along c , the set of Bragg reflections can be divided into three distinct categories:⁷¹

- Main reflections, $hk00$, are generated when the incident beam is collinear to the incommensurate c -axis; since both substructures have a common periodicity in the ab -plane, these reflections are generated by scattering off both substructures.
- Reflections specific to one composite substructure will have either $l \neq 0$ or $m \neq 0$; reflections generated by scattering off the first (Co-B) substructure will have indices $hkl0$, while those generated by scattering off the second (Mg) substructure will have indices $hk0m$.
- Satellite reflections, $hklm$ ($l \neq 0$ and $m \neq 0$), may be observed where both substructures contribute to scattering of incident beam not parallel to the c -axis. This can only be the case when scattering factors of one substructure are modulated by the periodicity of the other substructure. For this class, a reflection $hklm$ will

be an m^{th} order satellite of the first substructure and an l^{th} order satellite of the second substructure.

In the contrasting case of incommensurately modulated crystals with one modulation vector and no separate composite parts, the Bragg reflections are simply split into two categories: $m = 0$ (main reflections) and $m \neq 0$ (satellite reflections). In many discussions, this scheme is extended to the case of incommensurate composite crystals where the reflections $hk0m$ are treated as “satellites” of the first composite part and reflections $hkl0$ as “satellites” of the second composite part. It should be noted that the term “modulation vector” may be misleading: in many cases, structural parameters such as atomic coordinates and displacement parameters may indeed be modulated incommensurately according to this vector, but this is not necessarily the case. Only when structure parameters of one substructure are modulated by the other are satellite reflections $hklm$ (of the third category) observed.

While the formalism necessary to describe such an incommensurate composite structure may seem cumbersome, there are several advantages to using a higher-dimensional model instead of a supercell approximant. Supercell descriptions for crystals of the same family differing only in the relative periodicities of the two subsystems can vary drastically, often adopting different space groups, Bravais lattice types, or even crystal systems,^{40,42,72} while the superspace symmetry descriptions of the average structures would be identical, differing only with respect to the value of the modulation vector. Furthermore, such a model alone would be applicable to a case for which the supercell approximant is too large to be practical. Any modulation of structure parameters from the basic structure is treated separately from the refinement of average atomic coordinates, which makes clear the extent of the mutual interaction of the two substructures. Finally, even in the case of a composite crystal with several modulation waves refined, there would be far fewer free parameters than in the case of a supercell approximant, leading to a more stable refinement.⁷³

Rietveld Refinement from Neutron and X-ray Diffraction Data. The Rietveld refinement of a $(3 + 1)D$ model in superspace with neutron and synchrotron powder XRD data was performed using the JANA2006 software.⁵⁸ At first, a Le Bail fit with one superspace dimension was accomplished to refine unit cell parameters and one modulation vector; refined values were in close agreement with the initial estimates given above derived from observed shifts of $hk5$ peaks in the orthorhombic model. A Rietveld refinement of the incommensurate composite model was then performed using NPD data (Figure 3), yielding a good fit of all the observed peaks aside from a few that were identified as arising from admixture phases. Figure S5 displays close-up views showing good agreement between predicted and observed profiles at low and high scattering angles. The peaks that were formerly indexed as $hk5$ with respect to the orthorhombic supercell and were observed at higher angles than predicted are now indexed as $h'k'01$ and are well-described in terms of both position and intensity.

For the NPD refinement, eight background coefficients and six parameters for the pseudo-Voigt peak shape function were refined, as well as phase fractions of impurity phases Mg (3.9 wt %), MgO (2.34 wt %), and MgCo_3B_2 (2.7 wt %) (see also Table S4). Positions of Co and B were refined, while Mg coordinates are constrained by symmetry. Although slight

discrepancies remain with respect to shapes and intensities of a few low-angle peaks, we attribute this to the complex angle-dependence of peak shape at POWGEN not being adequately modeled, even with six pseudo-Voigt parameters (to our knowledge JANA2006 is not capable of modeling angle-dependent profile parameters in a time-of-flight refinement). Importantly, the neutron powder diffraction profile lacks the high background caused by incoherent scattering of ${}^1\text{H}$ characteristic of samples with significant amounts of hydrogen, confirming that hydrogen from the magnesium hydride precursor does not play a role in stabilizing the ternary phase.

We then attempted to use the same model to fit HR-PXRD data (Figure S6). For this refinement, four pseudo-Voigt peak shape function parameters were refined, and 12 additional background parameters had to be added to account for a broad peak from the silica capillary around $Q = 1.5 \text{ \AA}^{-1}$. This sample included admixture phases Mg (10.1 wt %) and MgO (6.8 wt %). Once again, the incommensurate composite model of the target phase accurately predicted all peak positions corresponding to both substructures, confirmed by the \mathbf{q} vector refining to nearly the same value for neutron and synchrotron powder diffraction data sets. Slight discrepancies in unit cell parameters might be attributed to data collection at different temperatures (Table S5). However, considerable discrepancies in peak intensity are observed between predicted and observed profiles, suggesting potential inadequacies in our model or the presence of stacking faults (*vide infra*). These discrepancies, which are more noticeable in the refinement from X-ray powder diffraction data, are assumed to stem from inconsistencies in the Co substructure, since Co is the strongest scatterer of X-rays and the weakest scatterer of neutrons relative to Mg and B. Attempts to improve the HR-PXRD fit by lowering symmetry proved to be unsuccessful (Note S3). Importantly, no evidence of peak splitting at high scattering angles is observed that would indicate slight divergence of a and b cell parameters (inset to Figure S6), so we are content to model $\text{Mg}_{1+\epsilon}\text{Co}_4\text{B}_4$ in high-symmetry tetragonal group $P4_2/nmc(00\gamma)s00s$.

Evaluation of Neutron and X-ray Refinement Results.

Although Stöger et al. recently reported on the structure of $\text{Y}_x\text{Os}_4\text{B}_4$ refined from SCXRD using a $(3 + 1)D$ incommensurate model, the structure of $\text{Mg}_{1+\epsilon}\text{Co}_4\text{B}_4$ as presented here was determined in ignorance of this report. Both compounds are essentially $\text{Nd}_{1+\epsilon}\text{Fe}_4\text{B}_4$ -type, yet differences exist between the two superspace models. Importantly, in the case of $\text{Y}_x\text{Os}_4\text{B}_4$, strong satellite reflections to the second order allowed for refinement of several higher-order modulation waves for Os, B, and Y positions as well as for Os ADPs. Because of the significant modulation of the [OsB] substructure, a different modulation vector \mathbf{q} gave a more convenient indexing of the strongest satellite reflections. This affected the choice of superspace basis vectors and the superspace group of the Os–B substructure (see Figures 1 and 2 of ref. 43). While in both cases the Mg or Y substructure was described in $P4_2/nmc(00\gamma)s00s$, the [OsB] substructure was described in $P4_2/nmc(00\gamma)00ss$ rather than $P4_2/nmc(00\gamma)s00s$. This discrepancy is discussed in Note S2. Despite the different formalisms for embedding the structure in superspace, the only essential difference between $\text{Y}_x\text{Os}_4\text{B}_4$ and $\text{Mg}_{1+\epsilon}\text{Co}_4\text{B}_4$ is the strong modulation observed for $\text{Y}_x\text{Os}_4\text{B}_4$.⁴³

Unit cell parameters and volumes of $\text{Mg}_{1+\epsilon}\text{Co}_4\text{B}_4$ as refined from neutron and X-ray diffraction data are in relatively good agreement, while the slightly smaller unit cell volume from the

Table 1. Unit Cell Parameters, Modulation Vector, Structural Parameters, and Refinement Statistics of $Mg_{1+\epsilon}Co_4B_4$ as Refined from NPD Data at 300 K

a , Å	c , Å	V , Å ³			q		
6.75847(7)	3.94007(8)	179.970(7)			1.2721(3) $\times c^*$		
atom	Wyckoff site	x_1/a	x_2/b	x_3/c_1	x_4/c_2	s.o.f.	U_{eq}
Composite Part 1, Superspace Group $P4_2/nmc(00\gamma)s00s$							
Co1	8i	0.12031(8) ^a	0.12031	0.6328(3) ^a		1	0.0017(6)
B1	8i	0.0727(1)	0.0727	0.1369(3)		1	0.0034(2)
Composite Part 2, Superspace Group $P4_2/nmc(00\gamma)s0s0$							
Mg1	2b	3/4	1/4		1/4	1	0.0121(10)
all reflections		N(obs)	511	R_F (obs)	7.85%		
		N(all)	669	R_F (all)	8.50%	R_p	5.48%
composite part #1		N(obs)	331	R_F (obs)	7.19%	wR_p	5.76%
		N(all)	351	R_F (all)	7.91%	GoF	2.85
composite part #2		N(obs)	141	R_F (obs)	10.98%		
		N(all)	276	R_F (all)	11.71%		

^aRevised from HR-PXRD data; fixed for the NPD refinement. Uncertainties listed are from the HR-PXRD refinement.

single-crystal experiment may reflect the lower temperature at which the experiment was performed (Table S5). However, the coordinates of B atoms change considerably when allowed to refine freely in the HR-PXRD refinement when compared to the SCXRD and NPD refinement results, which are in relatively good agreement. Since B is the lightest atom and thus the weakest scatterer of X-rays in this compound, this discrepancy suggests that refinement of its position from HR-PXRD is not reliable. The coordinates of Co are in much closer agreement between NPD and both types of XRD data, although the values from neutron diffraction are assigned higher uncertainty than either of the X-ray techniques.

Refinement of atomic displacement parameters proved to be challenging for both NPD and HR-PXRD data. For the HR-PXRD data, all atomic displacement parameters tended to refine to negative values, while for the NPD data, displacement parameters for Co and B converged to small but reasonable values, while that of Mg was significantly larger (Table S5). Refinement of anisotropic harmonic displacement parameters for Co and B from neutron data gave reasonable U_{11} and U_{22} values but negative U_{33} and off-diagonal terms. Furthermore, refinement of anisotropic Mg displacement parameters for all three data sets yielded an ellipsoid that is extremely elongated along c , indicating that there may be additional structural displacement, ordered or disordered, of Mg along the direction of the channels. Free refinement of Mg occupancy and isotropic ADP, along with one modulation wave of occupancy, was attempted but did not significantly improve the fit or the refinement statistics. Extreme elongation of displacement ellipsoids of atoms occupying the R position in $NdCo_4B_4$ -type structures has been reported for several phases and may point to hidden incommensurate structural mismatch.^{74,75}

As noted above, the modulation vector q is remarkably consistent between the two refinements (Table S5), which is important as the value of q has a direct bearing on the composition of the phase. The value $|q|$ represents the ratio between the repeating length of the [CoB] (first) substructure and the repeating length of the Mg (second) substructure, such that $|q| \times c_2$ is the same length as c_1 . Since the crystallographic multiplicity of Co and B is four times greater than that of Mg, this also means that there are $|q| \times 1$ Mg atoms for every 4 × Co and B atoms, yielding an empirical formula $Mg_{1.272}Co_4B_4$. If the formula is represented as “ $Mg_{1+\epsilon}Co_4B_4$ ” after $Nd_{1+\epsilon}Fe_4B_4$, the value of ϵ is given by $\epsilon = |q| - 1 = 0.272$.

We did not find any evidence in either the NPD or the HR-PXRD profile of satellite reflections $hklm$ ($l \neq 0, m \neq 0$) or supercell reflections, which would indicate deviation of structure parameters from their average values in each subcell in an incommensurate or commensurate fashion, respectively. However, it should be noted that slight modulation of Mg structure parameters would lead only to weak satellite reflections, considering the greater scattering power of Co and B in X-ray and neutron experiments, respectively. In the cases of $R_{1+\epsilon}Fe_4B_4$ ($R = Ce, Pr, Nd, Gd, Ho$), $Sm_{1+\epsilon}Co_4B_4$, and $Pr_{1+\epsilon}Re_4B_4$, which were refined in commensurate supercells, superstructure reflections allowed refinement of commensurate positional modulation whereby T_4 tetrahedra ($T = Fe, Co, Re$) rotate slightly about the [001] axis, effectively easing certain close contacts between the substructures.^{38–40,66} Satellite reflections are commonly observed for incommensurate composite structures,⁷⁶ such as the misfit layer compounds^{71,77} and the large class of Nowotny chimney-ladder phases.^{72,73}

The relative independence of the Mg and Co–B substructures is corroborated by de Wolff sections of each atom type (Figures S7–S9), which represent contour lines of electron density summed from a Fourier calculation such that an atom's position along one spatial coordinate can be traced relative to the changing superspace coordinate. If substantial positional or ADP modulation were present, the de Wolff sections would show some combination of curves and disjunct line segments; instead, the contours are nearly straight. Figure S10 shows an x_3 – x_4 contour plot of Co and Mg scattering density and demonstrates how the crystal can be visualized as an intersection of 3D space with superspace as a horizontal line in superspace, with atomic positions in 3D space arising from the intersection of “strings” representing atoms in superspace with an arbitrary section of 3D space.

To report this incommensurate composite structure, we present a model where unit cell parameters, modulation vector, B coordinates and all isotropic atomic displacement values were refined from NPD data, with Co fixed in the position refined from HR-PXRD (where the uncertainty is much lower than when Co is refined freely against NPD data). We note that the slightly high U_{iso} value for Mg may point to underlying inadequacies in our model, potentially indicative of unmodeled disorder or distortion in the Mg substructure. These refined parameters together with refinement statistics are presented in Table 1; further details of the crystal structure refinement and

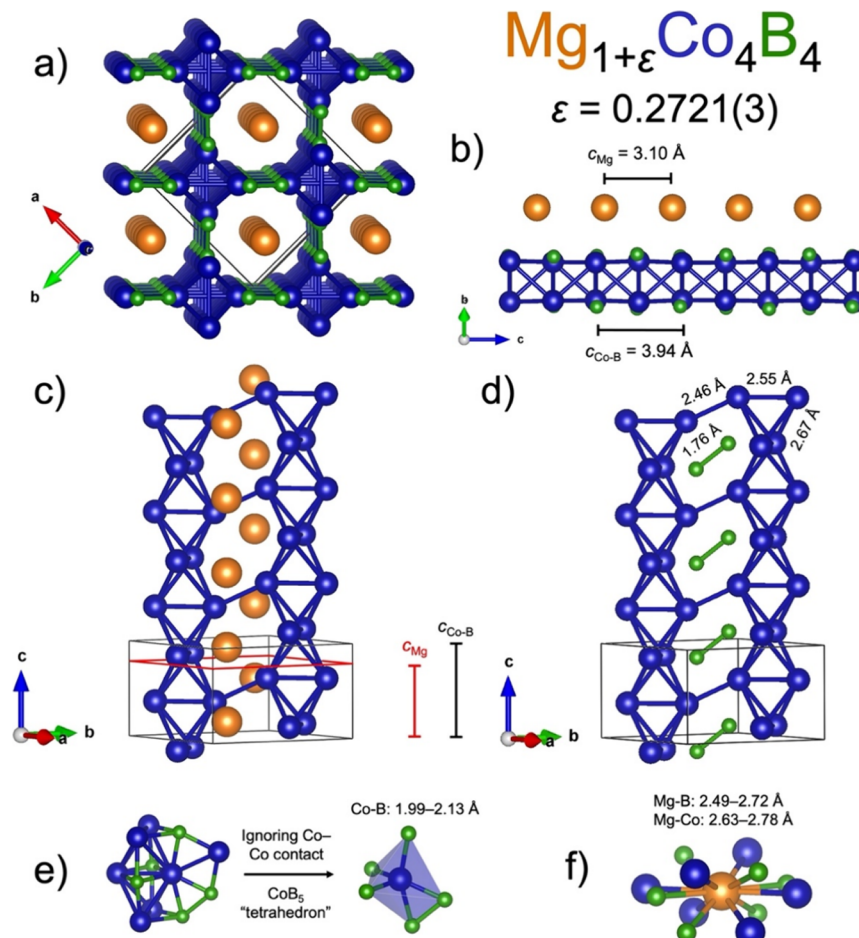


Figure 4. Crystal structure of $\text{Mg}_{1+\varepsilon}\text{Co}_4\text{B}_4$, showing (a) view down the c -axis with $[\text{CoB}]$ channel framework and linear Mg chains clearly visible, (b) mismatch in lattice parameter between the Mg and Co–B substructures, (c) arrangement of Mg atoms relative to chains of Co tetrahedra and superimposed unit cells of the two substructures, (d) arrangement of B–B dimers relative to chains of Co_4 tetrahedra and Co–Co and B–B separations, (e) coordination environment of Co and Co–B separations, and (f) one possible coordination environment of Mg with the closest possible Mg–B and Mg–Co separations in the xy -plane. Views showing atoms drawn with displacement parameters at 99% probability are shown in Figure S11.

a CIF file can be obtained from the Inorganic Crystal Structure Database (ICSD) from FIZ Karlsruhe – Leibniz Institute for Information Infrastructure (www.fiz-karlsruhe.de) by quoting the CSD 2484896 deposition number at www.ccdc.cam.ac.uk/structures. Since the sample used for neutron diffraction was prepared with isotopically pure ^{11}B , boron is the strongest scatterer of neutrons in our compound, while cobalt is the weakest. This is the reverse of the situation for X-rays, where scattering power increases as the square of the atomic number. This is therefore an example of a system of elements where X-ray and neutron scattering techniques are complementary, as the strongest scatterers of one radiation type are the weakest of the other, and the two techniques used in tandem provide a more convincing model than would be possible when using one technique in isolation.

Crystal Structure Description. In the $\text{Nd}_{1+\varepsilon}\text{Fe}_4\text{B}_4$ family of compounds, deviation of the periodicities of the two substructures from the commensurate case of NdCo_4B_4 results in the incorporation of excess R , quantified by the parameter ε . The value of ε for these compounds depends on the relative sizes of the R and T atoms, ranging from 0.093 observed for $\text{Nd}_{1+\varepsilon}\text{Fe}_4\text{B}_4$ ⁴¹ to 0.171 for $\text{Pr}_{41}(\text{Mn}_4\text{B}_4)_{35}$.³⁸ In the structure of $\text{Mg}_{1+\varepsilon}\text{Co}_4\text{B}_4$, on the other hand, where a much smaller atom

(Mg) occupies the channels, the favorable distance between atoms within the channels decreases while the distance from Mg to Co or B becomes longer relative to the sum of the respective atomic radii, weakening the interactions between the channel atoms and the T–B framework. Both the greater independence of the two substructures and the energetic favorability of short Mg–Mg separations serve to reduce the impetus for the two substructures to align commensurately. Furthermore, the relatively small size of Mg should lead to minimal positional modulation of the T–B substructure, observed for $R_{1+\varepsilon}\text{Fe}_4\text{B}_4$ compounds in cases where large R atoms impinge on nearby Fe clusters.^{38,39}

As noted above, the absence of true satellite reflections ($hklm$, $l \neq 0$ and $m \neq 0$) has led us to conclude that long-range modulation of structure parameters of one substructure by the other is below the detection limit of the diffraction methods employed. In the following crystal structure description, we will therefore first treat the two substructures independently, then consider the nature of the interactions between them. Note that in the superspace model, only one independent crystallographic site exists for each atom type.

A series of views of the crystal structure of $\text{Mg}_{1+\varepsilon}\text{Co}_4\text{B}_4$ are shown in Figure 4. As described above, Co and B atoms form a

three-dimensional framework creating channels along the *c*-direction that are occupied by Mg atoms, as made clear by the view down the [001] direction in Figure 4a. The backbone of this Co–B framework is the infinite chains of Co tetrahedra that set this structure type apart from the other *RT*₄B₄ structure types; these chains, stretching along the *c*-direction, are visible in Figure 4b and c. Figure 4b highlights the independent periodicities of the Mg and Co–B substructures; the separation shown between the substructures is to scale and emphasizes the relative isolation of the Mg atoms from the Co–B framework. In Figure 4c, the two distinct unit cells are shown to emphasize that the two substructures have a shared periodicity in the *a*- and *b*-directions and differ only in the *c*-direction; the connections between adjacent Co chains (through Co–Co bonds and B–B dimers) are shown. Ignoring the relatively longer contacts to Mg, Co is in an 11-coordinate environment, bonding to five B atoms and six other Co atoms (Figure 4e). If the Co–Co contacts are also ignored, Co is found connected to four boron dimers: three with the dimer roughly head-on (so Co approaches only one of the B atoms) and one with Co roughly equidistant to both B atoms. If the interaction of Co with this dimer is treated as one bond, the coordination of Co by B is effectively tetrahedral, i.e. CoB₃(B₂), with Co–B distances ranging between 1.99 Å and 2.13 Å (Figure 4e). Separations between Co atoms range from 2.46 Å for the connections between the chains of Co tetrahedra to 2.55 and 2.67 Å within the chains (Figure 4d). As seen in Figure 4d, the bridging Co–Co bonds between adjacent chains form cavities in the shape of an elongated hexagon. B–B dimers with a separation of 1.76 Å are found to lie within these cavities (Figure 4d). Note that, when viewed along the *c*-axis, the B–B dimers are aligned along the [110] direction in accord with the mirror symmetry normal to (*a* + *b*) in *P*4₂/*ncm* (Figure 4a), in contrast to the NdCo₄B₄ structure type where the B dimers (and *T* tetrahedra) rotate slightly about the [001] direction (Figure 1c), resulting in the lower symmetry group *P*4₂/*n*. The observed Co–B, Co–Co, and B–B distances are comparable to those found in Co₂B (Co–Co = 2.426 Å, Co–B = 2.150 Å) and MgCo₃B₂ (Co–Co = 2.442–2.537 Å, Co–B = 2.034–2.242 Å, B–B = 1.870 Å).³² Even shorter B–B dimers (1.42–1.54 Å) are observed for the LuRu₄B₄ and LuRh₄B₄ structure types (Figure 1b),⁷⁸ but these are well below the ICSD average of 1.75 Å.⁷⁹

The Mg substructure consists of infinite chains of Mg atoms separated by 3.099 Å in the *c*-direction. The separation between Mg atoms in adjacent chains, 5.024 Å, is too long for any significant interaction to occur. The Mg–Mg separation within the chains is slightly shorter than that of Mg metal (3.200 Å) and slightly longer than that of MgCo₃B₂ (2.926 Å), a compound which also contains Mg atoms occupying infinite linear channels in a Co–B framework.³²

Because the Mg atoms can occur at any *z*-coordinate relative to the [CoB] substructure the separation between Mg atoms and Co and B may vary over a continuous range of values with a lower bound but no upper bound. The possible range of these distances can be represented in a *t*-plot (Figure S12), where the parameter *t* represents the initial phase of the modulation wave vector and ultimately derives from the fact that points *x*₁^A and *x*₁^B differing by a lattice translation in 3D space will be modulated differently according to their different superspace coordinate *x*₄. In an incommensurate composite structure, varying *t* has the effect of changing the relative origins of the two substructures (Figure S13). In Figure S12,

between 0 and 1 is plotted on the abscissa and Mg–B and Mg–Co separations are plotted on the ordinate. Evaluation of a structural parameter (e.g., ADP parameters, atomic separation) between *t* = 0 to *t* = 1 gives the range of possible values for that parameter for any alignment of the two substructures relative to each other.

In the *t*-plot, the curves for Mg–B distances show a minimum separation of 2.4876 Å for four values of *t*, while the curves for Mg–Co distances indicate a minimum separation of 2.6274 Å at the same *t* values. This means that Mg is at its closest separation from B and Co for nearly the same *t* value, which is consistent with adjacent Co and B atoms differing in relative *z*-coordinate by only 0.004. Although intermetallic compounds with both Mg and Co are scarce, this minimum possible Mg–Co separation is comparable to that in MgCoGe (2.795 Å),⁸⁰ MgCo₃C (2.701 Å),⁸¹ and MgCo₃B₂ (2.685 Å).³² These Mg–B and Mg–Co minimum separations will also be compared to the minimum separations found in several supercell models (*vide infra*) that effectively incorporate positional modulation to lengthen contacts between the substructures.

Transmission Electron Microscopy. Scanning transmission electron microscopy was used to obtain high-angle annular dark-field (HAADF-STEM) images as shown in Figure 5, overlaid with calculated images generated from a 5:4

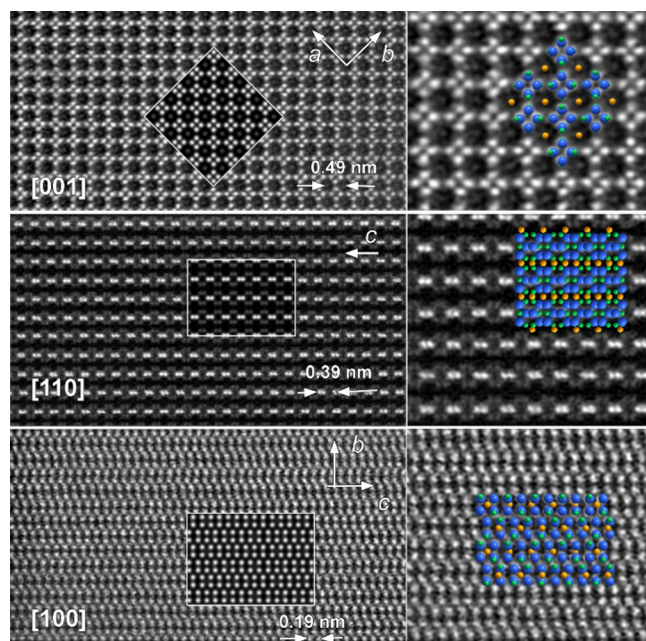


Figure 5. HAADF-STEM images overlaid with structural model (Co: blue, Mg: orange, B: green) and calculated images generated from a 5:4 supercell model showing views along the [001], [110], and [100] zone axes.

supercell model. The view of Mg_{1+*e*}Co₄B₄ down the [001] zone axis (top) clearly shows a channel structure with atoms residing in the center of the channels. In HAADF-STEM images, the contrast depends on the thickness (or the number of atoms within an atomic column) and atomic number ($\sim Z^2$). Therefore, atoms with larger *Z* are brighter and light atoms are invisible; in the present case, the bright atoms forming the framework are Co (*Z* = 27) and the less bright atoms inside the channels are Mg (*Z* = 12). The views along

the [001], [110] and [100] zone axes show generally good agreement with the simulated images. All images along main zone axes show good crystallinity and are generally free of defect structure. However, images along [401] zone axis revealed the presence of stacking faults (Figure S14). The presence of stacking faults could provide an explanation for the mismatch in peak intensities observed in the Rietveld refinement of HR-PXRD data.

Electron diffraction (ED) patterns along the main and most informative crystallographic zone axes are shown in Figure 6.

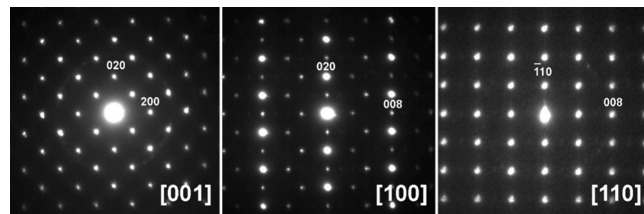


Figure 6. Electron diffraction patterns along [001], [100] and [110] zone axes confirming tetragonal metric symmetry and showing evidence of satellite reflections and kinematically absent reflections ($0k0, k \neq 2n$) likely due to double diffraction in the [100] ED pattern. Diffraction spots are indexed according to a 5:4 supercell approximant with cell parameters $a = b = 6.758 \text{ \AA}$ and $c = 15.760 \text{ \AA}$.

All ED patterns can be indexed based on a 5:4 tetragonal supercell with cell parameters $a = b = 6.758 \text{ \AA}$ and $c = 15.760 \text{ \AA}$. A 4-fold axis is seen in the [001] pattern, confirming the tetragonal symmetry of the structure. Reflections ($0k0, k \neq 2n$) violate the conditions for the n glide plane in $P4_2/nmc(00\gamma)$ s00s and are not seen in any neutron or X-ray scattering experiments. These spots are seen in the [100] image but not the [001] image, suggesting that they likely originate from double diffraction due to the dynamical nature of electron scattering,⁸² where the condition for double diffraction is not fulfilled in the case of the [001] axis. This is confirmed by a tilting experiment (Figure S15), where conditions for double diffraction are suppressed.

In addition to the main reflections with $l = 4n$ according to the 5:4 supercell, a set of reflections forming a zigzag shape (circled in red in Figure 7g) is seen in the [100] pattern that take odd l values with respect to the supercell. These reflections corroborate the incommensurate nature of the structure since they cannot be indexed to the reciprocal lattice of the small [CoB] subcell, where $l_{\text{CoB}} = 4 \times l$ with respect to the 5:4 supercell. Such reflections therefore arise from the Mg substructure ($l = 5n$) or interactions between the two substructures ($l \neq 4n$ or $5n$). In the case of the isostructural $\text{Nd}_{1+\epsilon}\text{Fe}_4\text{B}_4$ series of compounds ($0.093 \leq \epsilon \leq 0.128$), a similar pattern of spots not observed in X-ray diffraction data was attributed by Zhao et al. to dynamical multiple scattering effects, presumably across the two substructures.^{41,42} However, in the present case, the same pattern is seen in the Fourier-transform of the [100] STEM image (Figure 7g), suggesting that the origin of these extra spots is inherent to the structure itself. Close inspection of HAADF-STEM and annular bright-field scanning transmission electron microscopy (ABF-STEM) images (Figure 7a–d) revealed occasional variation in the intensity of regions where Mg atoms are present in the channels between pairs of Co atoms (circled in red in Figure 7c and d). The periodic variation in the alignment of Mg with the motif of pairs of Co atoms is scarcely visible in the

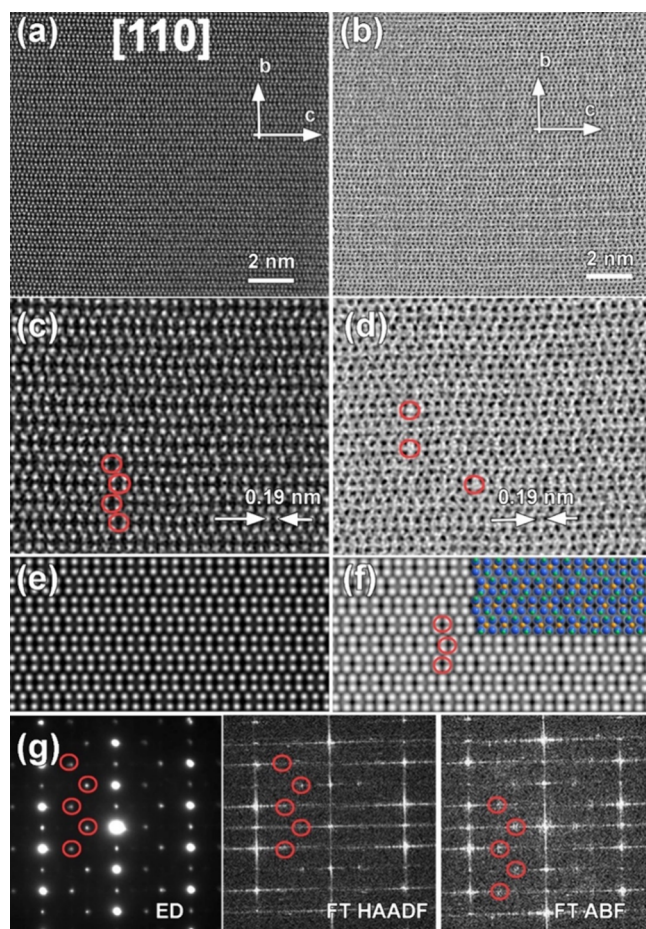


Figure 7. HAADF-STEM (a) and ABF-STEM (b) images taken along the [100] zone axis showing irregularities within the channels—variation in the level of contrast in regions between Co pairs (indicated by red circles) shown in magnified HAADF (c) and ABF (d) images, presumably due to absence of Mg atoms at that position; simulated [100] HAADF-STEM image (e) and the same simulated image with enhanced brightness and overlaid structural model from 5:4 supercell (f), where darker contrast dots (marked with red circles) correspond to Mg-free areas; electron diffraction pattern along [100] and FT patterns of HAADF-STEM and ABF-STEM images (g), where red circles highlight the additional spots.

calculated HAADF-STEM image (Figure 7e) but becomes apparent when the contrast is enhanced (Figure 7f, red circles). Therefore, we hypothesized that the extra spots were due to an additional periodicity or modulation to the Mg substructure. Adding a modulation wave to the position or occupancy of the Mg site did not yield the correct pattern of additional spots, while adding a modulation wave to the Co position provided the closest pattern to that observed by ED and FFT-STEM (Figure S16). In such a model, the modulation of the Co–B substructure obeys the periodicity of the Mg substructure. Presumably, the modulation affects the B positions as well due to the strong covalent nature of the Co–B interactions (*vide infra*), explaining why the additional spots are observed in the Fourier transform of both HAADF and ABF images. Although this pattern of satellite reflections hints at the existence of positional modulation of the Co–B substructure, it was not possible to refine the values of the modulation parameters because these satellite reflections were too weak in the neutron or X-ray powder diffraction data.

High-Temperature Powder X-ray Diffraction. In situ synchrotron powder X-ray diffraction was used to probe the behavior and stability of presynthesized $Mg_{1+\epsilon}Co_4B_4$ under conditions of elevated temperature (Figures S17, S18). Discussion of the sequential Rietveld refinement used to determine coefficients of thermal expansion can be found in Note S4, Table S6 and Figure S19. Values of the \mathbf{q} vector were refined for selected patterns between 300 and 1100 K using the superspace model (Table S6). γ , the z -component of \mathbf{q} remains relatively constant near its initial value up to 700 K, then drops abruptly and tends toward 1.25 at 800 K and above. This indicates an increase in the c_2 cell parameter governing the Mg–Mg spacing in the channels, which in turn implies a slight loss of Mg from the channels, potentially due to reaction of Mg with the silica capillary. Similarly, the intensity of the (1001) reflection drops gradually up to 800 K, then becomes noticeably stronger above 800 K (Figure S20). Both these features suggest that, rather than a gradual and consistent leaching of Mg atoms from the structure, the $Mg_{1+\epsilon}Co_4B_4$ phase transforms to a commensurate structure above 800 K with composition $Mg_{1.25}Co_4B_4$, since a value of $\mathbf{q} = 1.25 \times c^*$ corresponds exactly to a 5:4 supercell (as in the Ccce model solved from SCXRD with empirical formula $Mg_5Co_{16}B_{16}$).

DFT Calculations. Because compounds with higher-dimensional crystallographic order are difficult to model computationally, three related commensurate structural models were evaluated using DFT for energetic stability and magnetic order: $MgCo_4B_4$, $Mg_8Co_{28}B_{28}$, and $Mg_5Co_{16}B_{16}$ (Figure S21). $MgCo_4B_4$ is the simplest commensurate case where $\mathbf{q} = c^*$, i.e. the c parameters for both substructures are identical, and $Mg_8Co_{28}B_{28}$ is an 8:7 commensurate supercell as observed for $Gd_{1+\epsilon}Fe_4B_4$. Likewise, $Mg_5Co_{16}B_{16}$ is a 5:4 commensurate supercell similar to the orthorhombic supercell solved from SCXRD. To construct these last two models, the [CoB] composite part is repeated seven (or four) times along c , then chains of eight (or five) Mg atoms are added with the appropriate periodicity. The positions of the atoms in the 5:4 supercell model drift slightly from their idealized positions after DFT relaxation. The effect of these atomic shifts is to lengthen the closest Mg–B and Mg–Co contacts, similar to what is observed for the supercell models of certain $R_{1+\epsilon}T_4B_4$ compounds.^{38–40,66} Refer to Table S7 and the associated discussion in the Supporting Information for a comparison of the closest Mg–Co and Mg–B contacts between several supercell models and the incommensurate composite model.

Table 2 shows the convex hull distance (E_d) and magnetic state for three different structures of $Mg_{1+\epsilon}Co_4B_4$, ordered from

Table 2. Comparison of Convex Hull Distance (E_d) as well as the Predicted Magnetic State for Three Commensurate Approximant Models of $Mg_{1+\epsilon}Co_4B_4$

model	Z	hull distance (E_d), eV/atom	magnetic state
$Mg_5Co_{16}B_{16}$	4	0	NM
$Mg_8Co_{28}B_{28}$	2	0.0065	NM
$MgCo_4B_4$	2	0.0277	NM

Mg-rich to Mg-poor. The Mg–Co–B ternary convex hull is constructed by including the formation energy of all known phases and the three model structures. Reference elemental and binary phases are obtained from the Materials Project database.⁸³ The structure for the $MgCo_3B_2$ phase is adopted from the $ZrCo_3B_2$ -type structure with the lowest energy at the

1–3–2 composition according to our previous study.³² Among the three commensurate approximants, the experimentally determined supercell with composition $Mg_5Co_{16}B_{16}$ is a stable phase and part of the convex hull. Therefore, it is the second theoretically stable Mg–Co–B ternary phase identified. The Mg-poor $MgCo_4B_4$ ($NdCo_4B_4$ structure type) is found to be thermodynamically least stable. Nevertheless, the hull distance of all the three model structures is quite small. Table S8 gives the formation energies as calculated with respect to the constituent elements normalized to the number of atoms and number of Co atoms per unit cell. The experimentally determined supercell with composition $Mg_5Co_{16}B_{16}$ displays the lowest formation energy.

With respect to magnetism, the spin-polarized DFT calculations do not yield a stable magnetic solution for any model. The partial DOS per Co atom from the non-spin-polarized density of states (DOS) for $Mg_5Co_{16}B_{16}$ (see Figure S22) does not satisfy the Stoner criterion to generate ferromagnetism. Thus, the nonmagnetic state for this system predicted by DFT calculations aligns with the experimental result indicating temperature-independent paramagnetism with no magnetic ordering down to 5 K (*vide infra*).

Projected crystal orbital Hamilton populations (–pCOHP) were calculated for each pair of atomic interactions in the ordered 5:4 supercell $Mg_5Co_{16}B_{16}$ (Figures S23, S24) to assess the extent and nature of covalent bonding interactions. Interestingly, the Co–Co interactions have a positive contribution well below E_F and a large negative contribution just below and at E_F , leading to a relatively low integrated COHP (–ICOHP) value (Table S9) and suggesting that the Co framework does not actually form the “backbone” of the structure from a chemical bonding perspective. It is known that a concentration of antibonding states at E_F for metal atoms can render them unstable with respect to ferromagnetic splitting of spin populations, e.g. for elemental Fe, Co, and Ni⁸⁴ as well as certain transition metal borides.⁸⁵ Although such an effect is not observed for $Mg_{1+\epsilon}Co_4B_4$, partial substitution of Co by electron-poor Mn or Fe would lower E_F further into the antibonding region, increasing the likelihood of ferromagnetic order.

The relative strength of the covalent contribution to each pairwise interaction was assessed by integrating the –pCOHP functions over a selected energy range to yield the –ICOHP (Table S9). The largest –ICOHP values are found for pairs involving boron: similar to the trigonal planar B_4 units in $Ti_{1.6}Os_{1.4}RuB_2$,⁸⁶ the B–B dimers exhibit strong bonding behavior with an –ICOHP of 6.47 eV/bond. On the other hand, the Mg–Mg interactions are the smallest overall, as minimal covalent interaction is expected for a chain of electropositive atoms. Overall, the pairs of atoms spanning the two substructures (Mg–B and Mg–Co) show small –pCOHP, underlining the relative independence of the two substructures.

The realization of a $Nd_{1+\epsilon}Fe_4B_4$ -type channel structure with an alkaline-earth atom in the R site raises the question of mobility of the Mg atoms for deintercalation and diffusion, considering the relatively low degree of covalent interaction between Mg atoms and the [CoB] framework (as well as neighboring Mg atoms). Recent theoretical exploration of the Mg–Fe–B and Li–Fe–B systems has identified other stable and metastable phases with $NdCo_4B_4$ or $Nd_{1+\epsilon}Fe_4B_4$ structure types.^{87,88} The authors investigated the mobility of the alkali atom within the channels by using *ab initio* molecular dynamics

(AIMD) to simulate the diffusion of Mg atoms within the channels. AIMD simulations on the series of $Mg_{1+\epsilon}Fe_4B_4$ compounds with limiting values $\epsilon = 0$ and $\epsilon = 1/7$ yielded diffusion coefficients between 1×10^{-5} and $5 \times 10^{-5} \text{ cm}^2/\text{s}$, with a specific charge capacity of 184 mAh/g for the $\epsilon = 0$ case and higher values for the incommensurate variants with increased Mg content.⁸⁷ Similar simulations for $Li_3Fe_8B_8$ (i.e., $Li_{1+\epsilon}Fe_4B_4$ with $\epsilon = 0.5$, a commensurate superstructure crystallizing in space group $P\bar{4}2_1c$) give an even higher diffusion coefficient of $D = 6.2 \times 10^{-4} \text{ cm}^2/\text{s}$, with a low diffusion barrier of 0.02 eV based on Arrhenius fitting of temperature-dependent simulations.⁸⁸

$Mg_{1+\epsilon}Co_4B_4$ composed of similar elements and adopting essentially the same structure as these computationally predicted compounds, is likely to display similar electrochemical and ionic transport behavior. To underline this, we calculated $-pCOHP$ curves and $-ICOHP$ values for $MgFe_4B_4$ and $Li_3Co_8B_8$ presented in comparison with $Mg_5Co_{16}B_{16}$ in Figures S23 and S24. Qualitatively, the $-pCOHP$ curves for analogous pairs of atoms are very similar, with the most prominent differences discussed below. To evaluate the ease of removal of the alkali atom from the structure, we focus on the relative strength of the interactions spanning the two substructures ($A-T$ and $A-B$, Figure S23, Table S9). $A-B$ covalent interactions are the stronger of the two, but the magnitude of these interactions is nearly identical for all three compounds (Table S9). These observations imply that the mobility of Mg in $Mg_5Co_{16}B_{16}$ should be comparable to that of the Mg atoms in $MgFe_4B_4$ and Li atoms in $Li_3Fe_8B_8$ showing high ionic conductivity in AIMD simulations. Indeed, since $Mg_{1+\epsilon}Co_4B_4$ is truly an incommensurate phase, we anticipate the two substructures to be even less strongly interacting than the commensurate approximations used for calculations. In all cases, the high $-ICOHP$ for $B-B$ and $T-B$ interactions (Table S9) implies that the [TB] framework should be robust and able to tolerate a high degree of deintercalation of A, essential for conduction of ions in electrochemical applications. We note that the metallic nature of all these phases makes them better suited to serve as electrode or conductive additive materials in Mg or Li battery construction rather than as solid-state electrolytes. Future work will explore the deintercalation and electrochemical behavior of $Mg_{1+\epsilon}Co_4B_4$. Beyond electrochemical applications, the potential ambient-condition superionic transport properties and the underlying mechanisms in this class of quasi-one-dimensional channeled structures are of great interest.

Magnetic Measurements. Measurements of field- and temperature-dependent magnetization on multiple samples of $Mg_{1+\epsilon}Co_4B_4$ reveal low magnetic susceptibility with little variation between 50 and 300 K (Figure S25) and linear increase in magnetization at high field (Figure S26). These features suggest temperature-independent (Pauli) paramagnetism of the bulk $Mg_{1+\epsilon}Co_4B_4$ phase. The small increase in magnetization at low field at both 5 and 300 K in the isothermal magnetization data suggest a small amount of a ferromagnetic admixture reaching saturation magnetization; otherwise, the increase in magnetization is linear with field, with no substantial change in slope between 5 and 300 K, as expected for a temperature-independent paramagnet (Figure S26). The small magnitude of χ across all measured temperatures (Figure S25) and the very low magnetization of $0.002 \mu_B/\text{Co}$ at high field underline the lack of long-range magnetic order in $Mg_{1+\epsilon}Co_4B_4$. The temperature-independent

nature of the observed paramagnetism is borne out by the magnetic susceptibility measurements at 1000 Oe applied field, where the variation in susceptibility at low temperature is small compared to the magnitude of susceptibility at 300 K ($\chi(300 \text{ K}) = 0.002 \text{ emu}/(\text{mol K})$; see Figure S25). Impurity phases are presumed to be responsible for the observed deviations from ideal temperature-independent behavior. The nature of these admixtures and their relative contributions to the magnetometry measurements are discussed further in the Supporting Information. Pauli paramagnetic behavior is consistent with the metallic nature predicted for related compounds $MgCo_3B_2$ and $MgFe_4B_4$.^{32,87} In the sample without evidence of MgB_2 impurity, no superconducting transition was observed down to 5 K, consistent with the trends in the $ErRh_{4-x}Co_xB_4$ system where 30 at. % Co is observed to quench superconductivity.³⁷

CONCLUSIONS

Rapid screening of compositional space with high temperature *in situ* powder X-ray diffraction using alkali/alkaline-earth hydrides as precursors in solid-state reactions has enabled the discovery and characterization of novel ternary boride $Mg_{1+\epsilon}Co_4B_4$. This compound is the second to be reported in the Mg–Co–B system and one of few ternary borides featuring an alkali/alkaline earth metal and a first-row transition metal. The (3 + 1) dimensional structure of $Mg_{1+\epsilon}Co_4B_4$ was solved from a combination of single-crystal XRD, high-resolution synchrotron XRD, and neutron powder diffraction and confirmed using scanning transmission electron microscopy and electron diffraction. Like the other members of the RT_4B_4 family, the basic structural units of $Mg_{1+\epsilon}Co_4B_4$ are transition metal tetrahedra and boron dimers; in particular, the structure of $Mg_{1+\epsilon}Co_4B_4$ is an incommensurate modification of the $NdCo_4B_4$ structure type and is isostructural to $Nd_{1+\epsilon}Fe_4B_4$ and several other members where $T = Fe, Mn$, or Re . $Mg_{1+\epsilon}Co_4B_4$ is the first example in the RT_4B_4 family of structures where Mg occupies the R position, but in contrast to the $Nd_{1+\epsilon}Fe_4B_4$ -type compounds, the Mg atoms within the channels are independent of the framework and do not cause positional modulation of the Co tetrahedra. Unlike many members of the RT_4B_4 family, which exhibit magnetic order and/or superconductivity at low temperature, no evidence of a superconducting or magnetic ordering transition is observed down to 5 K. The observed temperature-independent paramagnetism is in agreement with DFT calculations performed on a commensurate superstructure predicting a nonmagnetic state. Substitution of Co for other first-row transition metals will be explored with the goal of accessing magnetically ordered states that may provide fertile ground for exploring quantum phenomena associated with the onset of magnetic order. Furthermore, future work will explore the possibility of removal of labile Mg cations from the channel structure through soft-chemical routes, potentially accessing metastable binary or ternary borides that are impossible to achieve from a high-temperature reaction.

ASSOCIATED CONTENT

SI Supporting Information

The Supporting Information is available free of charge at <https://pubs.acs.org/doi/10.1021/jacs.5c16523>.

Additional tables, plots, and discussion of structural refinements from SCXRD, HR-PXRD, and NPD;

discussion of the $(3 + 1)D$ symmetry of $Mg_{1+\epsilon}Co_4B_4$; final refinement parameters for the structural model of $Mg_{1+\epsilon}Co_4B_4$; de Wolff sections and plots of interatomic separations vs t ; comparison of HAADF-STEM with FFT and ED for selected zone axes; plots and refined parameters from the in situ PXRD experiment; results of DFT calculations; magnetic measurements ([PDF](#))

Accession Codes

Deposition Number [2484896](#) contains the supplementary crystallographic data for this paper. These data can be obtained free of charge via the joint Cambridge Crystallographic Data Centre (CCDC) and Fachinformationszentrum Karlsruhe [Access Structures service](#).

AUTHOR INFORMATION

Corresponding Author

Julia V. Zaikina – Department of Chemistry, Iowa State University, Ames, Iowa 50011, United States;  [orcid.org/0000-0002-8755-1926](#); Email: yzaikina@iastate.edu

Authors

Paul Oftedahl – Department of Chemistry, Iowa State University, Ames, Iowa 50011, United States;  [orcid.org/0009-0007-0522-896X](#)

Gourab Bhaskar – Department of Chemistry, Iowa State University, Ames, Iowa 50011, United States

Nawsher J. Parvez – Department of Physics and Astronomy, University of Delaware, Newark, Delaware 19716, United States

Zhen Zhang – Department of Physics and Astronomy, Iowa State University, Ames, Iowa 50011, United States;  [orcid.org/0009-0001-0810-8054](#)

Yang Sun – Department of Physics, Xiamen University, Xiamen 361005, China

John Q. Xiao – Department of Physics and Astronomy, University of Delaware, Newark, Delaware 19716, United States;  [orcid.org/0000-0001-7805-8155](#)

Thomas Proffen – Neutron Scattering Division, Oak Ridge National Laboratory, Oak Ridge, Tennessee 37830, United States;  [orcid.org/0000-0002-1408-6031](#)

Oleg I. Lebedev – Laboratoire CRISMAT, ENSICAEN-CNRS, UMR 6508, 14050 Caen, France

Complete contact information is available at:

<https://pubs.acs.org/10.1021/jacs.5c16523>

Notes

The authors declare no competing financial interest.

ACKNOWLEDGMENTS

We thank Dr. Wenqian Xu at beamline 17-BM APS ANL, Dr. Andrey Yakovenko at beamline 11-ID-C APS ANL, and Dr. Melanie Kirkham at BL-11A (POWGEN) SNS ORNL for assisting with the in situ X-ray diffraction and neutron diffraction experiments, respectively. We thank Dr. Adam Leontowich at WLE BXDS CLS for assistance with planning and completing the high-resolution powder X-ray diffraction experiment, Prof. Kirill Kovnir and Dr. Gayatri Viswanathan (Chemistry, Iowa State University and Ames National Laboratory) for access to PXRD instruments and discussions, and Dr. Cinthia Antunes Corrêa and Dr. Václav Petříček (Institute of Physics, Czech Academy of Sciences) for assistance with JANA2006 software. Financial support from

the U.S. Department of Energy (DOE) Established Program to Stimulate Competitive Research (EPSCoR) Grant No. DE-SC0024284 is gratefully acknowledged. Part of this research was performed on APS beam time, including award <https://doi.org/10.46936/APS-189935/60014049> from the Advanced Photon Source, a U.S. Department of Energy (DOE) Office of Science user facility operated for the DOE Office of Science by Argonne National Laboratory under Contract No. DE-AC02-06CH11357. Part of the research described in this paper was performed at the Canadian Light Source, a national research facility of the University of Saskatchewan, which is supported by the Canada Foundation for Innovation (CFI), the Natural Sciences and Engineering Research Council (NSERC), the Canadian Institutes of Health Research (CIHR), the Government of Saskatchewan, and the University of Saskatchewan. A portion of this research used resources at the Spallation Neutron Source, a DOE Office of Science User Facility operated by the Oak Ridge National Laboratory. The beam time was allocated to POWGEN on proposal number IPTS-30733.1. Y.S. acknowledges the support from NSFC (T2422016).

REFERENCES

- (1) Herbst, J. F.; Croat, J. J.; Pinkerton, F. E.; Yelon, W. B. Relationships between Crystal Structure and Magnetic Properties in Nd₂Fe₁₄B. *Phys. Rev. B* **1984**, *29* (7), 4176–4178.
- (2) Nagamatsu, J.; Nakagawa, N.; Muranaka, T.; Zenitani, Y.; Akimitsu, J. Superconductivity at 39 K in Magnesium Diboride. *Nature* **2001**, *401*, 63–64.
- (3) Gabani, S.; Flachbart, K.; Siemensmeyer, K.; Mori, T. Magnetism and Superconductivity of Rare Earth Borides. *J. Alloys Compd.* **2020**, *821*, No. 153201.
- (4) Lamichhane, T. N.; Xiang, L.; Lin, Q.; Pandey, T.; Parker, D. S.; Kim, T. H.; Zhou, L.; Kramer, M. J.; Bud'ko, S. L.; Canfield, P. C. Magnetic Properties of Single Crystalline Itinerant Ferromagnet AlFe₂B₂. *Phys. Rev. Mater.* **2018**, *2* (8), No. 084408.
- (5) Tan, X.; Chai, P.; Thompson, C. M.; Shatruk, M. Magnetocaloric Effect in AlFe₂B₂: Toward Magnetic Refrigerants from Earth-Abundant Elements. *J. Am. Chem. Soc.* **2013**, *135* (25), 9553–9557.
- (6) Castro, P. B. de; Terashima, K.; Yamamoto, T. D.; Hou, Z.; Iwasaki, S.; Matsumoto, R.; Adachi, S.; Saito, Y.; Song, P.; Takeya, H.; Takano, Y. Machine-Learning-Guided Discovery of the Gigantic Magnetocaloric Effect in HoB₂ near the Hydrogen Liquefaction Temperature. *NPG Asia Mater.* **2020**, *12* (1), 35.
- (7) Zieschang, A. M.; Bocarsly, J. D.; Schuch, J.; Reichel, C. V.; Kaiser, B.; Jaegermann, W.; Seshadri, R.; Albert, B. Magnetic and Electrocatalytic Properties of Nanoscale Cobalt Boride, Co₃B. *Inorg. Chem.* **2019**, *58* (24), 16609–16617.
- (8) Lee, E.; Fokwa, B. P. T. Nonprecious Metal Borides: Emerging Electrocatalysts for Hydrogen Production. *Acc. Chem. Res.* **2022**, *55* (1), 56–64.
- (9) Janisch, D.; Igoa Saldaña, F.; De Rolland Dalon, E.; V. M. Inocencio, C.; Song, Y.; Autran, P. O.; Miche, A.; Casale, S.; Portehault, D. Covalent Transition Metal Borosilicides: Reaction Pathways in Molten Salts for Water Oxidation Electrocatalysis. *J. Am. Chem. Soc.* **2024**, *146* (31), 21824–21836.
- (10) Mohammadi, R.; Lech, A. T.; Xie, M.; Weaver, B. E.; Yeung, M. T.; Tolbert, S. H.; Kaner, R. B. Tungsten Tetraboride, an Inexpensive Superhard Material. *Proc. Natl. Acad. Sci. U. S. A.* **2011**, *108* (27), 10958–10962.
- (11) Pangilinan, L. E.; Hu, S.; Akopov, G.; Cabrera, S. C.; Yeung, M. T.; Mohammadi, R.; Tolbert, S. H.; Kaner, R. B. Superhard Materials: Advances in the Search and Synthesis of New Materials. In *Encyclopedia of Inorganic and Bioinorganic Chemistry*; Wiley, 2021; pp 1–13. .

- (12) Pangilinan, L. E.; Hu, S.; Hamilton, S. G.; Tolbert, S. H.; Kaner, R. B. Hardening Effects in Superhard Transition-Metal Borides. *Acc. Mater. Res.* **2022**, *3* (1), 100–109.
- (13) Akopov, G.; Yeung, M. T.; Kaner, R. B. Rediscovering the Crystal Chemistry of Borides. *Adv. Mater.*. Wiley-VCH Verlag June 6, 2017. .
- (14) Iyer, A. K.; Zhang, Y.; Scheifers, J. P.; Fokwa, B. P. T. Structural Variations, Relationships and Properties of M₂B Metal Borides. *J. Solid State Chem.* **2019**, *270*, 618–635.
- (15) Bolotina, N. B.; Dudka, A. P.; Khrykina, O. N.; Mironov, V. S. Crystal Structures of Dodecaborides: Complexity in Simplicity. In *Rare-Earth Borides*; Inosov, D. S., Ed.; Jenny Stanford Publishing: New York, 2021; pp 293–330. .
- (16) Jung, W.; Mirgel, R. Darstellung Und Kristallstruktur Des Natrium-Iridiumborids NaIr₃B₄. *Journal of the Less Common Metals* **1988**, *143* (1–2), 49–57.
- (17) Schweitzer, K.; Jung, W. Darstellung Und Kristallstruktur Der Isotypen Verbindungen Ca₂Os₃B₅ Und Eu₂Os₃B₅. *Z. Anorg. Allg. Chem.* **1986**, *533* (2), 30–36.
- (18) Rogl, P. Ternary Borides with Boron–Boron Chain Formation. In *Inorganic Reactions and Methods*; Zuckerman, J. J., Hagen, A. P., Eds.; John Wiley & Sons, Inc.: Hoboken, NJ, USA, 1991; Vol. 13, pp 147–156. .
- (19) Wind, J.; Romaniv, O.; Schöllhammer, G.; Bursik, J.; Michor, H.; Giester, G.; Rogl, P. The Systems Tantalum (Niobium)-Cobalt-Boron. *J. Phase Equilibria Diffus* **2014**, *35* (1), 43–85.
- (20) Sun, J.; Wang, R.; Ding, Z.; Zhang, X.; Zhang, Q.; Zhang, B.; Dong, H.; Wu, F. Layered Li-Co-B as a Low-Potential Anode for Lithium-Ion Batteries. *Inorg. Chem.* **2023**, *62* (21), 8136–8144.
- (21) Sun, J.; Wang, R.; Liang, Y.; Zhang, B.; Wu, F.; Dong, H. Layered Na-Ni-B with Low Volume Expansion for Sodium-Ion Batteries. *J. Phys. Chem. C* **2024**, 1288161.
- (22) Sun, Y.; Zhang, Z.; Porter, A. P.; Kovnir, K.; Ho, K. M.; Antropov, V. Prediction of Van Hove Singularity Systems in Ternary Borides. *NPJ. Comput. Mater.* **2023**, *9* (1). .
- (23) Zhang, Z.; Porter, A. P.; Sun, Y.; Belashchenko, K. D.; Viswanathan, G.; Sarkar, A.; Gamage, E. H.; Kovnir, K.; Ho, K.-M.; Antropov, V. Unveiling a Family of Dimerized Quantum Magnets, Conventional Antiferromagnets, and Nonmagnets in Ternary Metal Borides. *J. Am. Chem. Soc.* **2024**, *146* (24), 16878–16891.
- (24) Zhang, Z.; Belashchenko, K. D.; Antropov, V. High-Throughput Studies of Novel Magnetic Materials in Borides. *AIP Adv.* **2025**, *15* (3). .
- (25) Gvozdetskyi, V.; Hanrahan, M. P.; Ribeiro, R. A.; Kim, T. H.; Zhou, L.; Rossini, A. J.; Canfield, P. C.; Zaikina, J. V. A Hydride Route to Ternary Alkali Metal Borides: A Case Study of Lithium Nickel Borides. *Chem.—Eur. J.* **2019**, *25* (16), 4123–4135.
- (26) Gvozdetskyi, V.; Bhaskar, G.; Batuk, M.; Zhao, X.; Wang, R.; Carnahan, S. L.; Hanrahan, M. P.; Ribeiro, R. A.; Canfield, P. C.; Rossini, A. J.; Wang, C. Z.; Ho, K. M.; Hadermann, J.; Zaikina, J. V. Computationally Driven Discovery of a Family of Layered LiNiB Polymorphs. *Angewandte Chemie - International Edition* **2019**, *58* (44), 15855–15862.
- (27) Jung, W. Darstellung Und Kristallstruktur von MgNi₂SB₂ und Li_{1,2}Ni₂SB₂. *Z. Naturforsch.* **1977**, *32b*, 1371–1374.
- (28) Adeyemi, A. N.; Bhaskar, G.; Cox, T.; Hong, S.; Gvozdetskyi, V.; Zaikina, J. V. Hydride Precursors in Materials Synthesis. In *Comprehensive Inorganic Chemistry III, Third ed.*; Reedijk, J., Poeppelmeier, K. R., Eds.; Elsevier, 2023; Vol. 1–10, pp 128–146. .
- (29) Gvozdetskyi, V.; Sun, Y.; Zhao, X.; Bhaskar, G.; Carnahan, S. L.; Harmer, C. P.; Zhang, F.; Ribeiro, R. A.; Canfield, P. C.; Rossini, A. J.; Wang, C.-Z.; Ho, K.-M.; Zaikina, J. V. Lithium Nickel Borides: Evolution of [NiB] Layers Driven by Li Pressure. *Inorg. Chem. Front* **2021**, *8* (7), 1675–1685.
- (30) Bhaskar, G.; Gvozdetskyi, V.; Batuk, M.; Wiaderek, K. M.; Sun, Y.; Wang, R.; Zhang, C.; Carnahan, S. L.; Wu, X.; Ribeiro, R. A.; Bud'ko, S. L.; Canfield, P. C.; Huang, W.; Rossini, A. J.; Wang, C. Z.; Ho, K. M.; Hadermann, J.; Zaikina, J. V. Topochemical Deintercalation of Li from Layered LiNiB: Toward 2D MBene. *J. Am. Chem. Soc.* **2021**, *143* (11), 4213–4223.
- (31) Bhaskar, G.; Gvozdetskyi, V.; Carnahan, S. L.; Wang, R.; Mantravadi, A.; Wu, X.; Ribeiro, R. A.; Huang, W.; Rossini, A. J.; Ho, K. M.; Canfield, P. C.; Lebedev, O. I.; Zaikina, J. V. Path Less Traveled: A Contemporary Twist on Synthesis and Traditional Structure Solution of Metastable LiNi₁₂B₈. *ACS Materials Au* **2022**, 2614.
- (32) Oftedahl, P.; Parvez, N. J.; Zhang, Z.; Sun, Y.; Antropov, V.; Xiao, J. Q.; Zaikina, J. V. Venturing into Unexplored Phase Space: Synthesis, Structure, and Properties of MgCo₃B₂ Featuring a Rumped Kagomé Network. *Chem. Mater.* **2024**, *36* (19), 9834–9847.
- (33) Parthé, E.; Chabot, B. Crystal Structures and Crystal Chemistry of Ternary Rare Earth-Transition Metal Borides, Silicides and Homologues. In *Handbook on the Physics and Chemistry of Rare Earths*; Gschneider, K. A., Jr., Eyring, L., Eds.; North-Holland: Amsterdam, 1984; Vol. 6, pp 113–334. .
- (34) Grüttner, A.; Yvon, K. Lanthanum Ruthenium Boride, LaRu₄B₄. *Acta Crystallogr. B* **1979**, *35* (2), 451–453.
- (35) Alekseeva, A. M.; Leithe-Jasper, A.; Prots, Yu.; Schnelle, W.; Grin, Yu.; Antipov, E. V. New Scandium Rhodium Boride Sc₄Rh₁₇B₁₂ with a Framework Structure: Synthesis, Crystal Structure, and Properties. *Russian Chemical Bulletin* **2008**, *57* (3), 532–540.
- (36) Prozorov, R.; Vannette, M. D.; Law, S. A.; Bud'ko, S. L.; Canfield, P. C. Coexistence of Ferromagnetism and Superconductivity in ErRh₄B₄ Single Crystals Probed by Dynamic Magnetic Susceptibility. *Phys. Rev. B* **2008**, *77* (10), No. 100503.
- (37) Rogl, P.; Tondiglia, V.; De Long, L. E. Structural Properties and Anomalous Composition Dependences of the Superconducting Transition Temperature of RE(Rh,Co)4B₄ Alloys (RE ≡ Y, Er). *J. Alloys Compd.* **1992**, *181* (1–2), 311–319.
- (38) Givord, D.; Tenaud, P.; Moreau, J. M. Modulation of the Iron Tetrahedra Driven by Interactions with R Atoms in R₁ + EFe₄B₄ Compounds. *Journal of the Less Common Metals* **1986**, *115* (2), L7–L10.
- (39) Givord, D.; Tenaud, P.; Moreau, J. M. Refinement of the Crystal Structure of R₁ + EFe₄B₄ Compounds (R ≡ Nd, Gd). *Journal of the Less Common Metals* **1986**, *123* (1–2), 109–116.
- (40) Zavalij, P. Yu.; Mykhaleko, S. I.; Kuz'ma, Yu. B. New Incommensurate Structures of the Borides Pr₄₁(Mn₄B₄)₃₅ and Pr₇(Re₄B₄)₆. *J. Alloys Compd.* **1994**, *203*, 55–59.
- (41) Zhao, Z. B.; Xia, S. K.; Wang, C. R.; Ma, R. Z. Nd₁ + EFe₄B₄, a Novel System of Infinitely Adaptive Structures. *J. Phys.: Condens. Matter* **1989**, *1* (41), 7513–7520.
- (42) Zhao, Z. B.; Hong, S. Y. A Group Theoretical Consideration of the Diffraction Patterns of Nd_{1+ε}Fe₄B₄ Compounds. *J. Phys.: Condens. Matter* **1992**, *4* (47), 9221–9234.
- (43) Stöger, B.; Sologub, O.; Salamatka, L. The Incommensurate Composite Y_xOs₄B₄ (x = 1.161). *Acta Crystallogr. B Struct Sci. Cryst. Eng. Mater.* **2024**, *80* (6), 724–731.
- (44) van Smaalen, S. An Elementary Introduction to Superspace Crystallography. *Z. Kristallogr Cryst. Mater.* **2004**, *219* (11), 681–691.
- (45) van Smaalen, S. Incommensurate Crystal Structures. *Crystallogr. Rev.* **1995**, *4* (2), 79–202.
- (46) Huq, A.; Kirkham, M.; Peterson, P. F.; Hodges, J. P.; Whitfield, P. S.; Page, K.; Húgle, T.; Iverson, E. B.; Parizzi, A.; Rennich, G. POWGEN: Rebuild of a Third-Generation Powder Diffractometer at the Spallation Neutron Source. *J. Appl. Crystallogr.* **2019**, *52* (5), 1189–1201.
- (47) Kresse, G.; Furthmüller, J. Efficient Iterative Schemes for *Ab Initio* Total-Energy Calculations Using a Plane-Wave Basis Set. *Phys. Rev. B* **1996**, *54* (16), 11169–11186.
- (48) Blöchl, P. E. Projector Augmented-Wave Method. *Phys. Rev. B* **1994**, *50* (24), 17953–17979.
- (49) Perdew, J. P.; Burke, K.; Ernzerhof, M. Generalized Gradient Approximation Made Simple. *Phys. Rev. Lett.* **1996**, *77* (18), 3865–3868.

- (50) Monkhorst, H. J.; Pack, J. D. Special Points for Brillouin-Zone Integrations. *Phys. Rev. B* **1976**, *13* (12), 5188–5192.
- (51) Dronskowski, R.; Bloechl, P. E. Crystal Orbital Hamilton Populations (COHP): Energy-Resolved Visualization of Chemical Bonding in Solids Based on Density-Functional Calculations. *J. Phys. Chem.* **1993**, *97* (33), 8617–8624.
- (52) Deringer, V. L.; Tchougréeff, A. L.; Dronskowski, R. Crystal Orbital Hamilton Population (COHP) Analysis As Projected from Plane-Wave Basis Sets. *J. Phys. Chem. A* **2011**, *115* (21), 5461–5466.
- (53) Maintz, S.; Deringer, V. L.; Tchougréeff, A. L.; Dronskowski, R. Analytic Projection from Plane-Wave and PAW Wavefunctions and Application to Chemical-Bonding Analysis in Solids. *J. Comput. Chem.* **2013**, *34* (29), 2557–2567.
- (54) Maintz, S.; Deringer, V. L.; Tchougréeff, A. L.; Dronskowski, R. LOBSTER: A Tool to Extract Chemical Bonding from Plane-wave Based DFT. *J. Comput. Chem.* **2016**, *37* (11), 1030–1035.
- (55) Sheldrick, G. M. A Short History of SHELX. *Acta Crystallogr. A* **2008**, *64* (1), 112–122.
- (56) Sheldrick, G. M. Crystal Structure Refinement with SHELXL. *Acta Crystallogr. C Struct. Chem.* **2015**, *71*, 3–8.
- (57) Momma, K.; Izumi, F. VESTA 3 for Three-Dimensional Visualization of Crystal, Volumetric and Morphology Data. *J. Appl. Crystallogr.* **2011**, *44* (6), 1272–1276.
- (58) Petříček, V.; Dušek, M.; Palatinus, L. Crystallographic Computing System JANA2006: General Features. *Z. Kristallogr. Cryst. Mater.* **2014**, *229* (5), 345–352.
- (59) Petříček, V.; Palatinus, L.; Plášil, J.; Dušek, M. Jana2020 – a New Version of the Crystallographic Computing System Jana. *Z. Kristallogr. Cryst. Mater.* **2023**, *238* (7–8), 271–282.
- (60) Chupas, P. J.; Chapman, K. W.; Kurtz, C.; Hanson, J. C.; Lee, P. L.; Grey, C. P. A Versatile Sample-Environment Cell for Non-Ambient X-Ray Scattering Experiments. *J. Appl. Crystallogr.* **2008**, *41* (4), 822–824.
- (61) Weiland, A.; Frith, M. G.; Lapidus, S. H.; Chan, J. Y. In Situ Methods for Metal-Flux Synthesis in Inert Environments. *Chem. Mater.* **2021**, *33* (19), 7657–7664.
- (62) Toby, B. H.; Von Dreele, R. B. GSAS-II: The Genesis of a Modern Open-Source All Purpose Crystallography Software Package. *J. Appl. Crystallogr.* **2013**, *46* (2), 544–549.
- (63) Krause, L.; Herbst-Irmer, R.; Sheldrick, G. M.; Stalke, D. Comparison of Silver and Molybdenum Microfocus X-Ray Sources for Single-Crystal Structure Determination. *J. Appl. Crystallogr.* **2015**, *48* (1), 3–10.
- (64) Černý, R.; Bonhomme, F.; Yvon, K.; Fischer, P.; Zolliker, P.; Cox, D. E.; Hewat, A. Hexamagnesium Dicobalt Undecadeuteride Mg₆Co₂D₁₁: Containing [CoD₄]₅⁻ and [CoD₅]₄⁻Complex Anions Conforming to the 18-Electron Rule. *J. Alloys Compd.* **1992**, *187*, 233–241.
- (65) Kwei, G. H.; Morosin, B. Structures of the Boron-Rich Boron Carbides from Neutron Powder Diffraction: Implications for the Nature of the Inter-Icosahedral Chains. *J. Phys. Chem.* **1996**, *100* (19), 8031–8039.
- (66) Bezing, A.; Braun, H. F.; Muller, J.; Yvon, K. Tetragonal Rare Earth (R) Iron Borides, R_{1+x}Fe₄B₄ (E=0.1), with Incommensurate Rare Earth and Iron Substructures. *Solid State Commun.* **1985**, *55* (2), 131–135.
- (67) van Smaalen, S. Superspace Description of Incommensurate Intergrowth Compounds and the Application to Inorganic Misfit Layer Compounds. *Mater. Sci. Forum* **1992**, *100–101*, 173–222.
- (68) Yamamoto, A. Unified Setting and Symbols of Superspace Groups for Composite Crystals. *Acta Crystallogr. A* **1992**, *48* (4), 476–483.
- (69) Sun, J.; Lee, S.; Lin, J. Four-Dimensional Space Groups for Pedestrians: Composite Structures. *Chem. Asian J.* **2007**, *2* (10), 1204–1229.
- (70) *International Tables for Crystallography*; Hahn, Th., Ed.; International Union of Crystallography: Chester, England, 2006; Vol. A.
- (71) Jobst, A.; van Smaalen, S. Intersubsystem Chemical Bonds in the Misfit Layer Compounds (LaS)_{1.13}TaS₂ and (LaS)_{1.14}NbS₂. *Acta Crystallogr. B* **2002**, *58* (2), 179–190.
- (72) Grin, Y.; Niewa, R.; Lidin, S.; Lind, H.; Boström, M. Synthesis, Crystal Structure, Phase Relations and Chemical Bonding Analysis of the New Nowotny Chimney-Ladder Compound ZrBi_{1.62}. *Solid State Sci.* **2006**, *8* (10), 1173–1180.
- (73) Lidin, S.; Rohrer, F. E.; Lind, H.; Eriksson, L.; Larsson, A.-K. On the Question of Commensurability – The Nowotny Chimney-Ladder Structures Revisited. *Z. Kristallogr. Cryst. Mater.* **2000**, *215* (11), 650–660.
- (74) Rogl, P. The Crystal Structure of LaIr₄B₄, ThOs₄B₄, ThIr₄B₄ (NdCo₄B₄-Type) and URu₄B₄, UOs₄B₄ (LuRu₄B₄-Type). *Monatsh. Chem.* **1980**, *111*, 517–527.
- (75) Hiebl, K.; Sienko, M. J.; Rogl, P. Magnetic Behavior and Structural Chemistry of RE(Os, Ir)B₄ Borides (RE ≡ Rare Earth). *Journal of the Less Common Metals* **1981**, *82*, 21–28.
- (76) Righi, L.; Merlini, M.; Gemmi, M. High-Temperature Evolution of the Incommensurate Composite Crystal Ca_{0.83}CuO₂. *Crystals (Basel)* **2020**, *10* (7), No. 630.
- (77) Wiegers, G. A. Misfit Layer Compounds: Structures and Physical Properties. *Prog. Solid State Chem.* **1996**, *24* (1–2), 1–139.
- (78) Johnston, D. C. Superconductivity in a New Ternary Structure Class of Boride Compounds. *Solid State Commun.* **1977**, *24* (10), 699–702.
- (79) Zagorac, D.; Muller, H.; Ruehl, S.; Zagorac, J.; Rehme, S. Recent Developments in the Inorganic Crystal Structure Database: Theoretical Crystal Structure Data and Related Features. *J. Appl. Crystallogr.* **2019**, *52*, 918–925.
- (80) Hlukhyy, V.; Chumalo, N.; Zaremba, V.; Fässler, T. F. Syntheses and Structures of the Germanides CaNiGe and MgCoGe as Well as Chemical Bonding in CaNiGe and CaNi₂Ge₂. *Z. Anorg. Allg. Chem.* **2008**, *634* (8), 1249–1255.
- (81) Huettter, L. J.; Stadelmaier, H. H. Ternary Carbides of Transition Metals with Aluminum and Magnesium. *Acta Metall.* **1958**, *6*, 367–370.
- (82) Gjónnes, J.; Moodie, A. F. Extinction Conditions in the Dynamic Theory of Electron Diffraction. *Acta Crystallogr.* **1965**, *19* (1), 65–67.
- (83) Jain, A.; Ong, S. P.; Hautier, G.; Chen, W.; Richards, W. D.; Dacek, S.; Cholia, S.; Gunter, D.; Skinner, D.; Ceder, G.; Persson, K. A. Commentary: The Materials Project: A Materials Genome Approach to Accelerating Materials Innovation. *APL Materials*. American Institute of Physics Inc. **2013**.
- (84) Landrum, G. A.; Dronskowski, R. The Orbital Origins of Magnetism: From Atoms to Molecules to Ferromagnetic Alloys. *Angew. Chem., Int. Ed.* **2000**, *39* (9), 1560–1585.
- (85) Fokwa, B. P. T.; Samolyuk, G. D.; Miller, G. J.; Dronskowski, R. Ladders of a Magnetically Active Element in the Structure of the Novel Complex Boride Ti₃Fe₂Ru₁₈B₈: Synthesis, Structure, Bonding, and Magnetism. *Inorg. Chem.* **2008**, *47* (6), 2113–2120.
- (86) Fokwa, B. P. T.; von Appen, J.; Dronskowski, R. Synthesis of a Missing Structural Link: The First Trigonal Planar B₄ Units in the Novel Complex Boride Ti_{1+x}Os_{2-x}RuB₂ (x = 0.6). *Chem. Commun.* **2006**, *42*, 4419–4421.
- (87) Zhang, Z.; Chen, S.; Zheng, F.; Antropov, V.; Sun, Y.; Ho, K.-M. Accelerated Exploration of Empty Material Compositional Space: Mg–Fe–B Ternary Metal Borides. *J. Am. Chem. Soc.* **2024**, *146* (48), 33179–33192.
- (88) Chen, S.; Oftedahl, P.; Zhang, Z.; Wu, Z.; Jiang, J.; Antropov, V.; Zaikina, J. V.; Wu, S.; Ho, K.-M.; Sun, Y. Prediction of Li₃Fe₈B₈ Compound with Rapid One-Dimensional Ion Diffusion Channels. *Phys. Rev. Mater.* **2025**, *9* (10), No. 105403.